Characteristics and Source Regions of Slow Alfvénic Solar Wind Observed by Parker Solar Probe

Tamar Ervin [ID],[1,2] Kai Jaffarove [ID],[1,2] Samuel T. Badman [ID],[3] Jia Huang [ID],[2] Yeimy J. Rivera [ID],[3] and Stuart D. Bale [ID][1,2]

[1]*Department of Physics, University of California, Berkeley, Berkeley, CA 94720-7300, USA*
[2]*Space Sciences Laboratory, University of California, Berkeley, CA 94720-7450, USA*
[3]*Center for Astrophysics | Harvard & Smithsonian, 60 Garden Street, Cambridge, MA 02138, USA*

ABSTRACT

Using a classification scheme for solar wind type based on the heliocentric distance of the observation, we look at near perihelion observations from Parker Solar Probe Encounters Four to Fourteen to study the sources of the slow Alfvénic solar wind (SASW). Through Potential Field Source Surface (PFSS) modeling and ballistic mapping, we connect streams to their solar source and find that a primary population of SASW comes from small coronal holes (CHs) and their over-expanded boundaries, while a second population seems to emerge from non-CH structures potentially through interchange reconnection with nearby open field lines. This CH-like SASW shows larger expansion than the FSW, potentially indicating additional heating below the critical point leading to slower wind emerging from CH-like structures. We show that SASW emerging from CH-like structures shows stronger preferential acceleration of alpha particles (similar to the FSW) than the SASW emerging from non-CH structures, and that this is a velocity dependent phenomena as found in previous studies. To have additional confidence in our mapping results, we quantify the error on both the PFSS model and ballistic mapping and discuss how additional multi-point observations of plasma parameters and composition would allow us to better constrain our models and connect the solar wind to its source.

1. INTRODUCTION

The source regions of the solar wind have been a topic of interest to the space physics community for decades, and while the source of the fast solar wind (FSW) is well known to be coronal holes (CH) (McComas et al. 1998, 2008, and others), the source of the slow solar wind is still unresolved. The solar wind has traditionally been categorized by wind speed at 1AU: fast (speeds above 500 km s^{-1} at 1AU) and slow (speeds below 500 km s^{-1}), however more recent works have shown that the slow solar wind can be further categorized into slow Alfvénic solar wind (SASW) and classical slow solar wind (SSW) based on the Alfvénicity of the plasma (D'Amicis & Bruno 2015; Stansby et al. 2018; Stansby et al. 2020b; Ervin et al. 2024b, and others). This SASW shows similar properties to the fast solar wind specifically in terms of Alfvénicity (D'Amicis & Bruno 2015; Perrone et al. 2020; D'Amicis et al. 2021), alpha particle abundances (Ohmi et al. 2004; Ervin et al. 2024b), differential velocities (Stansby et al. 2020a), and composition (Stakhiv et al. 2015; D'Amicis et al. 2018; Ervin et al. 2024b) meaning that this wind likely has a similar source to the FSW (D'Amicis & Bruno 2015; D'Amicis et al. 2021, and others).

Since the FSW emerges from open field lines streaming from within CHs, some of the SASW likely originates from CHs and/or their boundaries (Wang & Sheeley 1990, and others). Expansion within these CH regions can play a role in the speed of the emergent wind and perhaps lead to slower wind emerging from CH regions. Specifically, heating above the critical point (where the wind becomes supersonic) increases wind speeds (Leer & Holzer 1980). Heating concentrated near the coronal base leads to a larger mass flux and lower energy available per particle which decreases the acceleration leading to slower wind speeds (Wang et al. 2009). Therefore, rapidly diverging fields with higher critical points and less energy deposited near the sonic point can produce slower speed winds (Wang et al. 2012; Stansby et al. 2020b).

The magnetic expansion factor (f_s) is a measure of the divergence of the magnetic field (Wang & Sheeley 1990, 1997) and there is an empirically established anti-correlation between the expansion factor and solar wind speed (Wang & Sheeley 1990). Small CHs and their boundaries have been shown to have higher magnetic expansion (Wallace et al. 2020; Ervin et al. 2024b) and could therefore be a source of slower wind due to higher critical points leading to heating

below the transition to supersonic wind speeds (Nolte et al. 1976; Garton et al. 2018). It has been shown that the expansion factor does not always follow this correlation with wind speed, but that the dynamic boundary between open and closed magnetic field lines could be responsible for this correlation or deviation from it (Riley et al. 2015; Wallace et al. 2020).

In addition to the correlation between expansion factor and wind type, different compositional characteristics have been shown to be associated with different wind speeds and a potential tracer of the source region of the wind. Due to the *freeze-in* process, composition ratios stay constant through the radial evolution of the solar wind and are thus a good metric to evaluate the source of the wind when compared with known properties of various source regions (Buergi & Geiss 1986; Chen et al. 2003; Landi et al. 2012). The processes that lead to compositional variations occur in the solar atmosphere itself, meaning that the amount of time spent in the corona will lead to differences in compositional metrics, and plasma must stay in the corona long enough (2-3 days) to experience these fractionation effects (Laming 2015). Therefore, plasma quickly escaping the corona on open field lines (such as from CH structures) show more 'photospheric' like compositions in comparison to plasma escaping from closed field lines or loop-like structures (Feldman & Marsch 1997; Laming 2017). These plasma parcels would show an enhancement in low first ionization potential (FIP) elements (high Fe/O ratio) and enhanced ion ratios arising from the hotter source region (Geiss et al. 1995; von Steiger et al. 2000).

The solar wind typically shows alpha particle (Helium; He) abundance ratios (A_{He}) that are depleted compared with photospheric values ($\sim$8.4%, Asplund et al. (2021)) and are highly variable. Helium rich periods are often associated with solar eruptions (Song et al. 2022; Feldman et al. 2005; Johnson et al. 2024), streamer belt outflows, and other active region structures (Kasper et al. 2016; Alterman et al. 2018; Alterman & Kasper 2019). There is some modulation of the abundance with the solar cycle which could be due to variations in the structure of the solar wind source regions throughout the solar cycle (Norton et al. 2023). Differences in A_{He} can also be attributed to gravitational settling, another process that shows solar cycle dependence (Rivera et al. 2022a). Therefore, even though Helium is the highest FIP element, the ubiquitously observed depletion of Helium within the ambient solar wind indicates that the process(es) leading to its enhancement or depletion are likely different from the FIP effect as described above (Johnson et al. 2024) and thus there is no full picture to describe what we would expect in terms of alpha abundance related to source region. Typically, A_{He} are expected to be enhanced in plasma streaming from open field lines or CH-like structures, however this does not always hold true (Ervin et al. 2024b).

In this study, we use Parker Solar Probe (Parker) observations within $40R_{\odot}$ from Encounters 4 to 14 to study the in situ characteristics and source regions of the SASW in comparison with the FSW, as the source region and characteristics of the FSW are well understood. We will not make any definitive claims regarding the general source of the SASW, but rather seek to highlight that they likely emerge from a variety of sources – some similar to FSW, some different. In Section 3, we outline our data selection and wind stream identification methods along with modeling methods we use to identify the source regions of the SASW streams of interest (additional details can be found in Appendix A). Section 4 discusses the in situ and modeling parameters associated with the SASW and identified source regions. We conclude in Section 5 with an overview of our results, the limitations of this study, and future work necessary to fully understand the source regions of the slow Alfvénic solar wind. In Appendix B we show overviews of modeling results for specific streams, and in Appendix C discuss uncertainty quantification on our modeling methods.

2. DATA OVERVIEW

This study uses observations from within $40R_{\odot}$ during Encounters 4 to 14 (E4 - 14) of Parker Solar Probe (Parker) spanning January 2020 to January 2023, providing a good overview of the solar wind at the inner heliosphere during solar minimum and into the rising phase of the solar cycle. We use near perihelion magnetic field measurements from the Electromagnetic Fields Investigation (FIELDS; Bale et al. (2016)) fluxgate magnetometer and partial plasma moments of alphas and protons from the ion Solar Probe ANalyzer (SPAN-I; Livi et al. (2022)) aboard the 'Solar Wind Electrons, Alphas, and Protons' (SWEAP; Kasper et al. (2016)) suite. SPAN-I measurements are available starting in Encounter 4 which is the reason observations from E1 to 3 are not used such that we can maintain consistency throughout our study, and use the native quality flags to mitigate field-of-view (FOV) issues. An important note is that the SPAN-I absolute abundance measurements (number density) is likely an underestimate of the total density as they are computed from partial moments (Livi et al. 2022).

As the lower boundary photospheric magnetic field observation to our potential field source surface (PFSS) modeling (described in Section 3.2), we use ADAPT-GONG magnetograms. These are high resolution, full disk photospheric

magnetograms from the Global Oscillation Network Group (GONG; Harvey et al. (1996)) with the Air Force Data Assimilative Photospheric Flux Transport (ADAPT; Worden & Harvey (2000); Arge et al. (2010, 2011, 2013); Hickmann et al. (2015)) model applied. To compare footpoints estimated from PFSS method, we use EUV observations from the Atmospheric Imaging Assembly (AIA; Lemen et al. (2012)) aboard the Solar Dynamics Observatory (SDO; Pesnell et al. (2012)), which takes high resolution and high cadence, narrow band full disk images of the solar atmosphere. We look at SDO/AIA observations of 193Å allowing us to probe EUV emissions in the corona with a characteristic $\log T$ of 6.3 (Lemen et al. 2012).

3. METHODS

3.1. *Stream Identification*

All usable (good field of view) E4 - E14 data within $40\text{R}_\odot$ was compiled and analyzed based on certain parameters. The objective of the method is to classify observed wind as SSW, SASW, or FSW. We can detect all three wind types simultaneously because the designated parameters are mutually exclusive such that each observation can belong only to a specific wind category.

It is common practice to identify slow solar wind as streams with mean speeds below a threshold value (typically 400 to 500 km s^{-1} depending on the heliocentric distance and study) for a specified time period. In this case, due to Parker being so close to the Sun, we modified the traditional classification scheme to account for solar wind acceleration. Using observations over more than a full solar cycle (2004 to 2024) from the Wind spacecraft (Lin et al. 1995) at 1AU, we looked at the fraction of the observed wind that would be considered classically fast. We then narrow this window to just the time period of the Parker observations we look at (January 2020 to January 2023) finding that $\sim 20\%$ was above 500 km s^{-1} and $\sim 50\%$ above 400 km s^{-1}. Appendix A shows an overview of this method and how these percentage thresholds stay consistent throughout time. We applied the categorization thresholds to Parker data observed at different radial distances.

Binning by radial distance in bins of $10\text{R}_\odot$ (10-20 $\text{R}_\odot$, 20-30 $\text{R}_\odot$, and 30-40 $\text{R}_\odot$) gave different thresholds for the fast versus slow solar wind cutoff depending on the radial distance. Wind is classified as 'slow' below 391 km s^{-1} from 10 - 20 $\text{R}_\odot$, 370 km s^{-1} from 20 - 30 $\text{R}_\odot$, and 388 km s^{-1} from 30 - 40 $\text{R}_\odot$, as seen in Figure 1. Applying these new thresholds for each radial bin, rather than the traditional classification, attempts to account for potential slow wind acceleration into fast wind beyond the location of Parker.
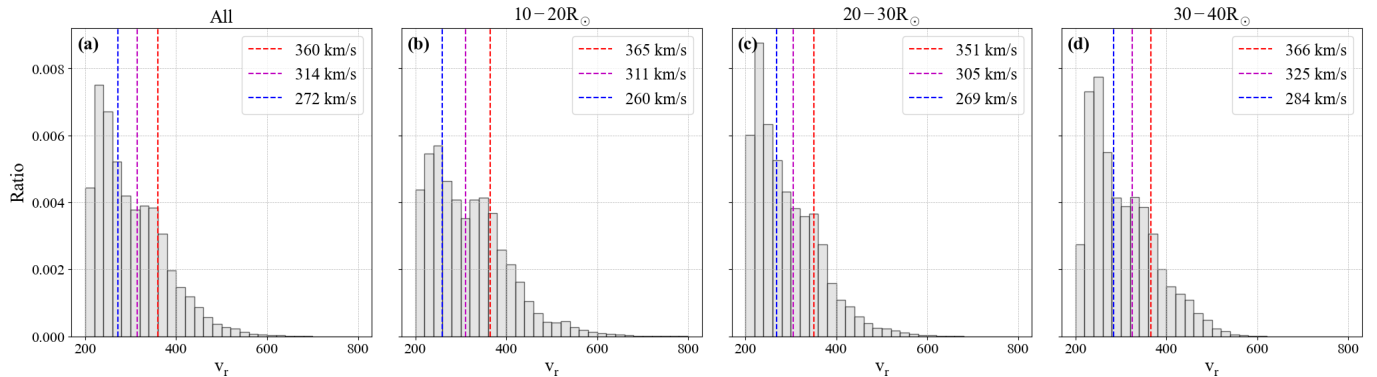

Figure 1. Distribution functions of solar wind speed binned by heliocentric distance. The dashed lines indicate different threshold percentages based on observations of wind speeds at 1AU (see section 3.1) as applied to Parker. The red, purple, and blue lines signify the uppermost 19%, 35%, and 51% of the wind respectively where 19% is the 500 km s^{-1} cutoff at 1AU, 51% is the 400 km s^{-1} cutoff, and 35% falls in between. In our data stream identification, we use the red line, or the fastest 19% of wind measured from Parker to differentiate slow and fast solar winds. The velocities associated with each dashed line are listed. *Panel (a):* All Parker solar wind velocity data below 40 $\text{R}_\odot$ for Encounters 4-14 with associated dashed lines. *Panel (b) - (d):* All Parker solar wind velocity data for radial bins (b): 10-20 $\text{R}_\odot$, (c): 20-30 $\text{R}_\odot$ and (d): 30-40 $\text{R}_\odot$ with the associated thresholds.

In addition to categorizing the wind by speed, we further categorize the slow wind into classically slow and slow Alfvénic wind based on the cross helicity (σ_C). σ_C is generally used as a proxy for the Alfvénicity of the plasma where

higher cross helicity measurements (σ_C values of 1 or -1) are indicative of pure Alfvén waves propagating parallel or antiparallel to the magnetic field. σ_C is calculated via Equation 1 where $E^\pm$ is the energy associated with the Elsässer variables: $\mathbf{z}^\pm = \delta\mathbf{v} \mp \text{sign}\langle B_r\rangle\delta\mathbf{b}$ such that $\text{sign}\langle B_r\rangle$ is the averaged polarity of the magnetic field. $< \cdots >$ represents a time average over a 60-minute non-overlapping time window which is based on the correlation times of Parker magnetic field fluctuations (Parashar et al. 2020; Chen et al. 2020) and captures the full spectral features over the inertial range (Ervin et al. 2024).

$$\sigma_C = \frac{< E^+ > - < E^- >}{< E^+ > + < E^- >} \tag{1}$$

We define slow wind to be Alfvénic (SASW) if every $|\sigma_C|$ value over a 30-minute time window is above 0.7, and considered classically slow (SSW) if it is below. This categorization method leads to three subcategories of wind based on the wind speed and σ_C value. We identify streams of interest as time intervals lasting at least 30 minutes that fall into one of these categories for the entire stream. Due to the trajectory of Parker, the streams will traverse different longitudinal/spatial distances depending on the portion of the trajectory to which the stream corresponds.

3.2. *Source Region Connection*

We use a combination of ballistic propagation (Snyder & Neugebauer 1966; Nolte & Roelof 1973; Badman et al. 2020; Macneil et al. 2022; Koukras et al. 2022) and potential field source surface (PFSS) modeling to connect the plasma observed at Parker to its estimated footpoint on the photosphere. The PFSS model is an efficient method to model the global coronal magnetic field out to an equipotential surface (source surface - R_{ss}) where the magnetic field is assumed to be purely radial. The model assumes a magnetostatic ($\nabla \times \mathbf{B} = 0$) corona, with a photospheric radial magnetic field observation as the inner boundary (Schatten et al. 1969; Altschuler & Newkirk 1969) to reconstruct the field out to the R_{ss}. We use the open source `sunkit-magex` [1] package (Stansby et al. 2020) to reconstruct the coronal field out to a R_{ss} height of 2.5$R_\odot$ (Hoeksema 1984) with ADAPT-GONG magnetograms as the inner boundary condition. We determine the best PFSS model for each encounter based on matching the observed neutral line (HCS) crossings at Parker with the modeled HCS from the PFSS instantiation (Badman et al. 2020; Ervin et al. 2024b).

The PFSS model only reconstructs the magnetic field out to the source surface (2.5$R_\odot$), and thus we need another method to connect the spacecraft trajectory which varies between 11$R_\odot$ and 40$R_\odot$ to the model outer boundary. Assuming a Parker spiral and varied wind speed (the in situ v_R measurement), we propagate the spacecraft trajectory down to the R_{ss} height to connect our observations with the model. This allows us to connect the plasma observed at Parker with its estimated footpoint location at the photosphere and identify source regions based on comparison with EUV images and other parameters.

In Appendix C we discuss model validation and sources of error in both the ballistic propagation and PFSS model. We find that the error in the estimated footpoints due to ballistic propagation methods is velocity dependent (impacting the slower wind more) and is on the order of 1°. For the PFSS modeling results, we find that the source surface height has the largest impact on the resulting footpoints, however this can be optimized by comparing modeled polarity with magnetic field observations. The choice of input magnetogram leads to an error of $\sim 2°$ when using magnetograms within a few days from the optimal input parameter. Neugebauer et al. (2002) showed that expected uncertainties in PFSS source region footpoints are $\sim 10°$ or less in longitude and while the error on the PFSS estimated footpoints is larger than for the ballistic propagation, the resulting source region is unaffected when using input parameters optimized to the observations leading to confidence in the results.

We use these modeling methods to closely examine 10 SASW streams and their sources in addition to the overall in situ characteristics of slow Alfvénic wind observed at Parker. We look at the source region and source characteristics of 5 FSW streams for comparison, as it has been well established that these streams emerge from CH regions and thus provide a good source of comparison for our modeled SASW streams (McComas et al. 1998, 2008).

In this paper, when we discuss coronal holes, we are referring to cool, low density regions of coronal plasma with rapidly expanding open field lines and low magnetic activity levels (Cranmer 2009). This manifests as relatively dark regions in EUV observations and low photospheric magnetic field values. When we refer to active regions (ARs), we are referencing regions of relatively high magnetic activity in the corona associated with strong photospheric magnetic fields in connection to bright loops in EUV (Weber et al. 2023).

---

[1] https://github.com/sunpy/sunkit-magex

4. DISCUSSION

4.1. *In Situ Characteristics*

As discussed in Section 1, the SASW shows high levels of Alfvénicity yet slow wind speeds. Along with the σ_C calculation, we can also determine the residual energy (σ_R) or the difference between the energy in velocity and magnetic field fluctuations, indicating which one is dominant in the plasma. $\sigma_R > 0$ is kinetic energy dominant plasma and $\sigma_R < 0$ is magnetic energy dominant. σ_R is calculated via Equation 2 where $< \cdots >$ represents a time average over a 60-minute non-overlapping time window (see Section 3.1). The Elsässer variables ($\mathbf{z}^\pm$) and their associated energies ($E^\pm$) are described in Section 3.1.

$$\sigma_R = \frac{2 < \mathbf{z}^+ \cdot \mathbf{z}^- >}{< E^+ > + < E^- >} \qquad (2)$$

Due to the relationship between σ_C and σ_R, we expect $\sigma_C^2 + \sigma_R^2 \leq 1$ (Bavassano et al. 1998) meaning these measurements (as shown in Figure 2) are bounded by a circle. A comparison of the three panels, each for a different wind categorization, shows the stark differences in the turbulence parameters between the types of wind. From panel (a), it is clear that the SSW shows dramatically different properties than the SASW (panel (b)) and FSW (panel (c)). The SSW shows a large variance in σ_R values, with the majority of the distribution at $\sigma_R < 0$, indicating the SSW is magnetically dominated and the σ_C distribution is concentrated between 0.5 and 0.7. We expect the cross helicity to be more strongly concentrated at $\sigma_C > 0$, as the solar wind at these heliocentric distances is dominated by outward propagating modes.

The SASW and FSW distributions look quite similar: $\sigma_R < 0$ and $|\sigma_C| \sim 1$, meaning that SASW and FSW are both magnetic energy dominant and the turbulence is strongly imbalanced: i.e. the energy fluxes in the inward and outward propagating wave modes ($E^\pm$) differ such that $\sigma_C \neq 0$ (Sioulas et al. 2024a). The impact of imbalance on higher-order turbulence statistics is an open area of investigation. Recent work by Shi et al. (2023); Sioulas et al. (2024a,b) and others have looked at the scaling of alignment angles, spectral indices, and the impact on the principles of 'critical balance' (Goldreich & Sridhar 1995, 1997) and 'scale-dependent dynamic alignment' (Boldyrev 2006; Chandran et al. 2015; Mallet & Schekochihin 2017) based on the level of imbalance.

The turbulence and energy properties of the SASW are far more similar to the FSW than the SSW, potentially indicating a similar source region and/or acceleration mechanism as the FSW (D'Amicis & Bruno 2015; D'Amicis et al. 2018; Stansby et al. 2020b; Ervin et al. 2024b).
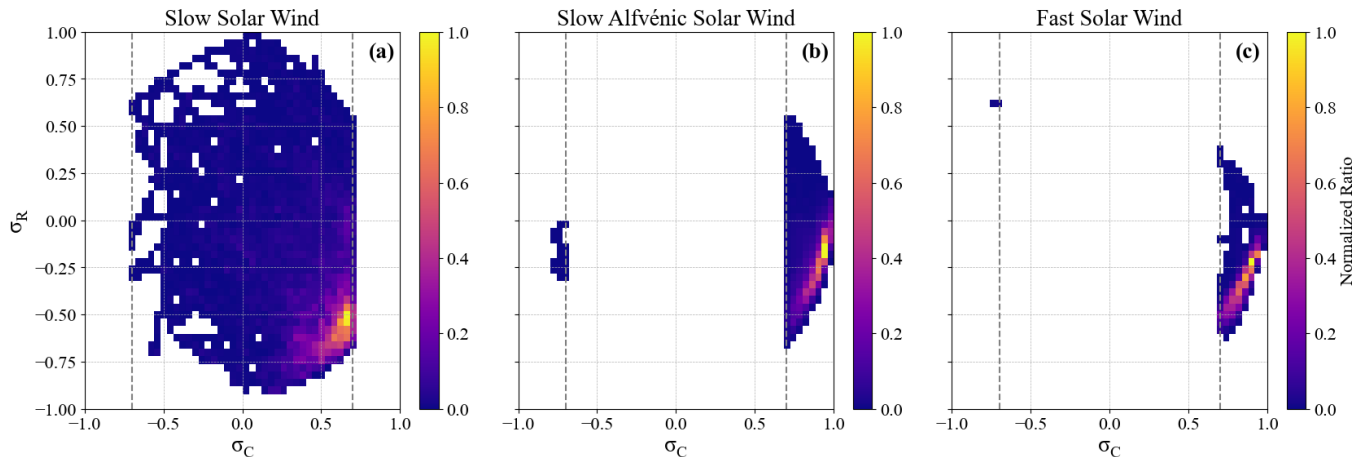

Figure 2. All usable E4 to E14 data (see Section 3.1) is compiled into normalized histograms of cross helicity (σ_C) against the residual energy (σ_R) to showcase the identification method. The criteria for categorization of 'high' Alfvénicity and the radially dependent velocity thresholding method are described in Section 3.1. Panels (a), (b), and (c) plot the designated data for SSW, SASW, and FSW respectively.

Classifying the solar wind into these categories allows us to study the sources and compositional metrics of these wind types. The alpha particle (Helium) abundance is the ratio of alpha particle and proton densities ($A_{He} = N_\alpha/N_p$).

Elemental composition is often used as a tracer of source region due to the conservation of plasma composition throughout the solar wind's radial evolution. Therefore, this can provide a helpful metric to compare between solar wind types in association with modeled source region mapping results. Generally, alpha particle abundances are shown to be solar cycle dependent in slow solar wind, ranging between $A_{He} \sim 1 - 4\%$, while abundances become less and less solar cycle dependent with increasing solar wind speed, remaining consistently around $A_{He} \sim 4\%$ (Kasper et al. 2007). In particular, He abundances exhibit the largest difference during periods around solar minimum/rising phase, where faster speed wind is observed to contain $A_{He} \sim 4\%$ while the slowest speed observed near the Earth contains 1%, making solar wind types the most distinguishable during this phase of the solar cycle. In general, alpha abundances are depleted compared with photospheric values, however, exhibit changes across solar wind values and thus can be used for analysis. Therefore, in this study that focuses on solar minimum and the rising phase, high A_{He} will likely be associated with open field line or CH-like structures where fast speed wind emanates from, however this is not always the case (see Section 1).

Figure 3 shows the proton and alpha particle composition for each wind type, where panel (a) looks at the SSW, panel (b) the SASW, and panel (c) the FSW. We include dashed lines at $A_{He} = 0.015$ and 0.045 to indicate the 'low' and 'high' abundance thresholds (Kasper et al. 2007; Kasper et al. 2012) and to guide the eye.

We see that the A_{He} for the SSW and SASW rarely cross the typical 'high abundance' threshold of 0.045 and that the SASW distribution is larger concentrated below the 'low abundance' boundary of 0.015. The SSW shows both intermediate and low alpha particle abundance. The FSW distribution clusters around the 'high abundance' threshold of 0.045 (as to be expected from CH wind), with some anomalous fast wind showing lower alpha densities than expected.
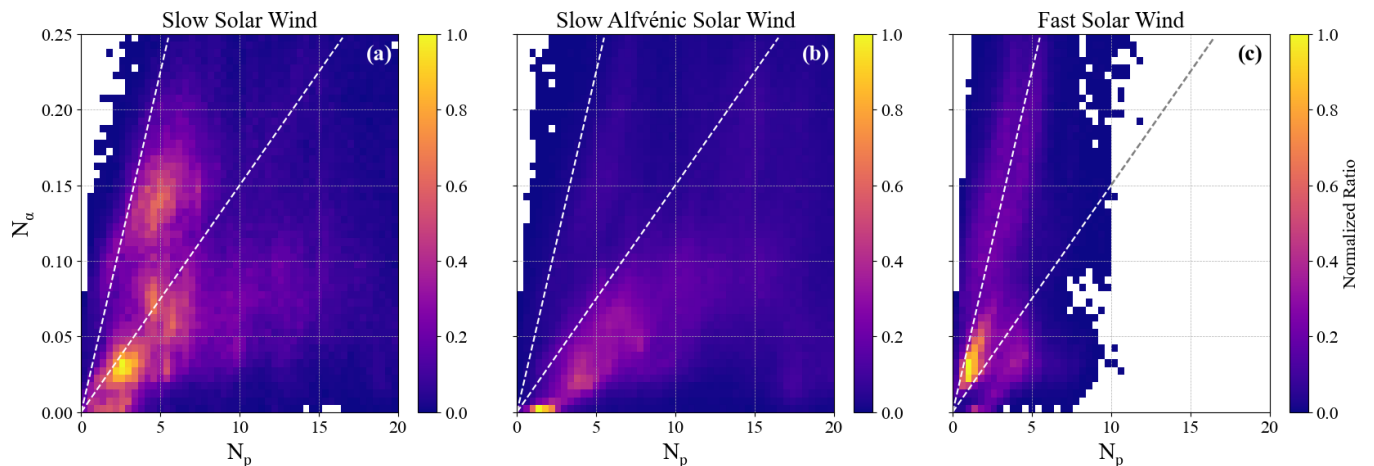
Figure 3. All usable E4 to E14 data (see Section 3.1) is compiled into these normalized histograms of alpha particle density (N_α) against proton density (N_p), each scaled by R^2. Particle measurements from the SPAN-I instrument aboard Parker/SWEAP show the alpha-to-proton abundance ratios. The dashed lines indicate the typical 'high helium abundance' threshold of 0.045 and the 'low abundance' boundary of 0.015 (Kasper et al. 2007; Kasper et al. 2012). Panels (a), (b), and (c) plot the designated data for SSW, SASW, and FSW respectively.

While the categorization of the slow wind by cross helicity is useful in creating to separate populations from potentially different sources, including compositional characteristics in categorization schemes would be a useful method to better categorize the wind by its source region. Additional observations of heavy ions and molecular composition would aid in this process allowing for better connection between in situ observations and sources, as our understanding of alpha particle abundance and its relation to source region is still convoluted and dependent on phase in the solar cycle.

The data highlighted above provides a strong rationale to study this additional categorization of the SASW due to its unique properties in energy and elemental composition in comparison to more classical fast and slow wind. The SASW is seen to have similar properties to the FSW in terms of σ_C and σ_R, supporting the evidence that at least some of SASW emerges from similar structures to the FSW. However, it is noteworthy that the observed alpha abundance for

Time Period	$\langle v_r \rangle$ [km s^{-1}]	$\langle |\sigma_C| \rangle$	$\langle M_A \rangle$	$\langle B_r R^2 \rangle$ [nT AU^2]	$\langle N_p R^2 \rangle$ [cm^{-3}]	$\langle B_0 \rangle$ [G]	$\langle f_{ss} \rangle$	$\langle I \rangle$
2020-01-28 18:00:00 to 2020-01-29 01:00:00 (E4)	284	0.86	2.06	-1.95	7.47	-4.27	236	30.9
2020-06-06 06:00:00 to 2020-06-06 09:00:00 (E5)	306	0.87	2.19	-2.03	6.77	-1.55	31.7	7.68
2020-06-09 03:00:00 to 2020-06-09 22:00:00 (E5)	217	-0.92	2.45	2.01	12.7	2.28	27.5	11.4
2020-09-27 12:00:00 to 2020-09-27 16:00:00 (E6)	306	-0.92	1.51	-2.12	7.54	-3.13	48.2	10.3
2021-01-18 18:00:00 to 2021-01-19 06:00:00 (E7)	231	0.86	2.29	-2.58	4.20	-5.86	27.7	23.6
2021-04-30 00:00:00 to 2021-04-30 05:00:00 (E8)	155	0.86	1.23	-1.99	20.6	37.8	105.7	395
2021-04-30 10:00:00 to 2021-05-01 00:00:00 (E8)	192	-0.95	1.70	-1.99	18.7	3.43	11.4	96.5
2022-12-10 18:00:00 to 2022-12-10 19:00:00 (E14)	187	-0.92	0.94	-2.65	17.9	-118	354	64.9
2022-12-10 20:30:00 to 2022-12-10 22:00:00 (E14)	178	-0.92	0.79	-2.81	16.7	-146	4798	596
2022-12-12 12:00:00 to 2022-12-12 16:00:00 (E14)	240	-0.90	1.36	2.56	16.6	-16.8	39	316

Table 1. Overview of the 10 SASW streams identified and modeled in this study. The $\langle \cdots \rangle$ refers to an average over these parameters for the entire stream. v_r, σ_C, M_A, $B_r R^2$ and $N_p R^2$ are parameters derived from in situ Parker measurements, while B_0, f_{ss}, and I are determined from the model estimated footpoints of the streams. B_0 is the photospheric footpoint field strength, f_{ss} is the magnetic expansion factor as defined by Equation 3, and I is the intensity of the footpoint from the corresponding AIA 193Å image.

the SASW is much lower than that of the FSW and the observed proton abundance is larger than the FSW (indicating additional mass flux), implying that some of this plasma likely has a unique source region or acceleration mechanisms, warranting additional study.

4.2. *Source Region Characteristics*

We use the PFSS and ballistic propagation methods for each Encounter to compare results produced from the 'estimated' footpoints for the SASW to the types of wind. We can calculate the expansion factor, photospheric magnetic field value at the footpoint, and brightness in EUV. Due to the inherent uncertainties in solar wind source modeling, doing this for one stream can be inconclusive and therefore we look at a variety of streams from E4 to E14 to have a more representative look at the potential sources of the SASW.

Based on the footpoint estimations, we can determine B_0 or the photospheric magnetic field value at the estimated point of plasma emergence by sampling GONG magnetograms at the footpoint locations. Additionally, we can calculate the magnetic expansion factor (f_{ss}) between the photosphere ($R_0 = 1.0R_\odot$) and another radial distance (R_1) based on Wang & Sheeley (1990, 1997):

$$f_s = \left(\frac{R_0}{R_1} \right)^2 \frac{B_R(R_0, \lambda_0, \phi_0)}{B_R(R_1, \lambda_1, \phi_1)} \tag{3}$$

such that expansion factor describes the divergence of the flux tube from spherical expansion ($f_s = 1$) meaning values of f_s greater than 1 indicate a rapidly diverging flux tube (Wang & Sheeley 1997). In this case, $R_1 = R_{ss}$, meaning our expansion factor is a measure of the expansion to the source surface: f_{ss}, which is the quantity previously correlation with heliospheric wind speed (Wang & Sheeley 1990; Riley & Luhmann 2012; Riley et al. 2015).

In Tables 1 and 2, we show an overview of the SASW and FSW streams we model and some of their associated characteristics.

The footpoint field strength can be used to differentiate between CH and non-CH regions. Stansby et al. (2021) studied the contribution of active regions to the solar wind over four solar cycles using GONG magnetograms (the same magnetograms used in this study). They set a lower limit on the field strength of ARs by looking at the maximum magnetic field strength outside of AR latitudes ($\pm 30°$ in the corona and $\pm 60°$ in the solar wind), finding it to be 30G for GONG, well above the established noise level of 3G (Clark et al. 2003). In Panel (a) of Figure 4, we look at the photospheric magnetic field strength at the footpoints for wind identified as fast and slow Alfvénic as described in Section 3.1. Using these methods, Ervin et al. (2024b); Ervin et al. (2024) looked at wind streams observed at Parker finding CH wind with $B_0 \sim 5\text{-}10$G and AR wind with footpoint strengths > 30G reaching ~ 73G. Similarly, Wang & Sheeley (2003) found that near solar maximum, slow wind streams emerge from small sheared regions near open field lines with high expansion factor ($f_{ss} > 10$) and high footpoint field strength ($B_0 > 30$G), while the fast wind streams come from regions of low expansion factor ($f_{ss} \sim 5$) and low photospheric fields ($B_0 \sim 5$G).

Time Period	$\langle v_r \rangle$ [km s^{-1}]	$\langle |\sigma_C| \rangle$	$\langle M_A \rangle$	$\langle B_r R^2 \rangle$ [nT AU^2]	$\langle N_p R^2 \rangle$ [cm^{-3}]	$\langle B_0 \rangle$ [G]	$\langle f_{ss} \rangle$	$\langle I \rangle$
2020-01-27 04:55:00 to 2020-01-27 05:15:00 (E4)	412	0.86	2.30	-2.18	3.78	-5.43	34.6	14.5
2021-04-27 01:00:00 to 2021-04-27 04:00:00 (E8)	436	0.86	1.54	-2.51	2.70	-15.1	75.5	81.7
2021-04-27 06:00:00 to 2021-04-27 08:30:00 (E8)	443	0.85	1.67	-2.45	3.25	-15.0	75.8	88.6
2021-11-20 05:30:00 to 2021-11-20 10:30:00 (E10)	563	0.88	1.48	-2.10	2.91	-12.9	34.4	34.8
2022-12-15 21:15:00 to 2022-12-15 22:15:00 (E14)	473	-0.80	2.21	3.47	3.36	17.0	15.9	126.7

Table 2. Overview of the 5 FSW streams identified and modeled in this study. The $\langle \cdots \rangle$ refers to an average over these parameters for the entire stream. v_r, σ_C, M_A, $B_r R^2$ and $N_p R^2$ are parameters derived from in situ Parker measurements, while B_0, f_{ss}, and I are determined from the model estimated footpoints of the streams. B_0 is the photospheric footpoint field strength, f_{ss} is the magnetic expansion factor as defined by Equation 3, and I is the intensity of the footpoint from the corresponding AIA 193Å image.

We find that the FSW streams show footpoint field strengths well below the 30G CH threshold, as expected. The overall distribution of modeled SASW streams also show footpoint field strengths below 30G, however when we look at the average values across individual streams (Table 1), we find that there are some streams where the average value exceeds (sometimes even dramatically) this threshold. We then further sub-divide our SASW streams into CH-like streams ($\langle B_0 \rangle$ below 30G) and non-CH streams ($\langle B_0 \rangle$ above 30G). With this reclassification, we now see a dramatic difference in the overall spread in the photospheric field strength, specifically the three 'non-CH' streams show B_0 values significantly higher than the CH threshold. The statistical separation of the in situ data (which is independent from our modeling results) bolsters confidence that the source mapping provides meaningful information, and indicates that there might be multiple source regions for the SASW, some similar to FSW sources (CHs and their boundaries) and some different.

Identical to our methods of sampling the GONG magnetograms at the estimated footpoint to determine B_0, we can sample EUV observations (SDO/AIA 193Å images) at these same footpoints to extract 'intensity' values. Brightness in EUV channels is dependent on the electron temperature and density, therefore hotter/denser ARs are brighter and cooler/tenuous CH structures are darker. We choose EUV images for comparison based on the estimated time the plasma left the photosphere which is determined based on the speed of the stream of interest and position of Parker. In Figure 5, we compare EUV intensity at the estimated footpoints of the 10 SASW streams we studied in depth, with the distribution of intensity values from a variety of AIA images corresponding to the two weeks around each of the studied SASW streams to give an overview of 'typical' distributions of intensity values. We find that the distribution of intensity values typically associated with SASW streams falls on the 'darker' (cooler) end of the distribution when compared with intensity values across many AIA images. Additionally, from Panel (b) of Figure 4, we see that the non-CH SASW shows much higher intensity values in comparison with the CH-like and FSW indicating a non-CH source.

From the PFSS method, we can also calculate the magnetic expansion factor, where a larger expansion factor implies more rapid divergence from spherical expansion ($f_{ss} = 1$). As discussed in the introduction, we would expect higher magnetic expansion factors from slow wind emerging from the same regions as fast wind, as rapid divergence of the flux tube leads to a higher critical point and thus the majority of the heating occurs below the transition to supersonic wind speeds (Leer & Holzer 1980). In Panel (c) of Figure 4, we find that in general the SASW has a higher expansion factor than the FSW. With our additional classification into CH-like and non-CH SASW, we find that the non-CH SASW has expansion factors an order of magnitude larger than the CH-like SASW and FSW. As shown in Figure 6, the non-CH wind has significantly larger mass flux which when coupled with the high expansion indicating a rapidly diverging field with a higher critical point, means more heating below the critical point leading to slower wind speeds. The same can be said for th CH-like SASW with its slightly higher mass flux and expansion, indicating that this is likely wind emerging from an overexpanded open field line in a CH-like region with additional heating below the critical point leading to slower wind speeds, but from the same structures as the FSW.

While anti-correlation between expansion factor and wind speed is expected (Wang & Sheeley 1990) and informs many current solar wind models such as the Wang-Sheeley-Arge (WSA) Model (Arge & Pizzo 2000; Arge et al. 2003; Arge et al. 2004) there is not a one-to-one correlation between speed and f_{ss}. Other models, such as the distance from the coronal hole boundary (DCHB) model (Riley et al. 2015) depend on the angular distance from a CH boundary
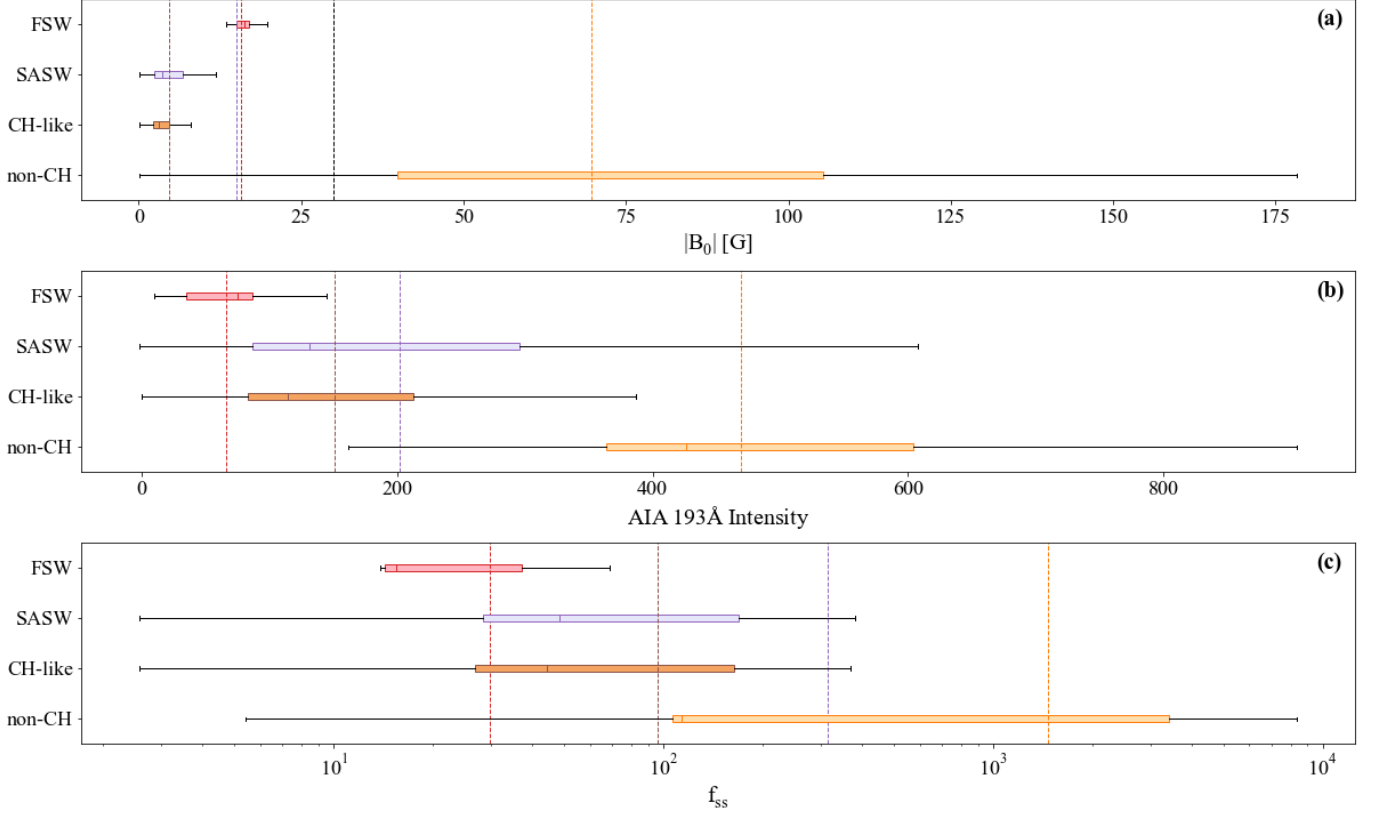
Figure 4. Overview of parameters determined from PFSS modeling and the associated estimated footpoints for the FSW. SASW, and the CH-like and non-CH SASW sub-categories. The boxplot shows the inner quartile range (25 - 75%) percentile and the solid line shows the median value. The dashed vertical lines show the mean of each parameter for the type of wind stream. Panels (a), (b), and (c) show the photospheric footpoint field strength (B_0), intensity at the footpoint from AIA 193Å images, and expansion factor based on Equation 3 respectively.

to determine the solar wind speed, rather than the expansion factor (Riley et al. 2001). This indicates that our understanding of the expansion and acceleration processes in the solar wind are incomplete, and relying solely on the expansion factor to infer a final wind speed is not a fully accurate description of the system.

Recent work by Yardley et al. (2024) combined spectroscopic observations with in situ measurements of plasma parameters and composition to find the emergence of wind streams from an AR-CH complex with an over-expanded magnetic field. They claim that coronal plasma trapped within closed loops can be released along open fan loops via interchange reconnection. Our observations of high expansion factors associated with high EUV intensity and strong footpoint magnetic field strength of these 'non-CH' streams alongside the long lived fan structures seen in EUV observations supports this idea (Fisk 2003). This would allow for plasma with non-CH composition to be released from coronal loop like structures after reconnection with open field lines leading to in situ composition observations different from the FSW. If we had measurements of heavy ion ratios and FIP bias from Parker, we would expect to see enhanced heavy ion ratios (O^{7+}/O^{6+}, C^{6+}/C^{4+}) and Fe/O ratios above typical photospheric values.

In Section 4.1, we looked at the overall distribution of proton and alpha particles from Parker observations. Now we will look at the composition of the modeled FSW and SASW streams in more detail to compare in situ metrics with potential sources. In Figure 6, we show an overview of the scaled proton density ($N_p R^2$), alpha particle abundance ($A_{He} = N_p/N_\alpha$), and normalized differential streaming speed ($\Delta v_{\alpha p} / v_A$) where $\Delta v_{\alpha p} = (v_\alpha - v_p)/\cos\theta$ ($\cos\theta = |B_R/B|$ to account for magnetic polarity). We find that the FSW streams have significantly lower proton densities and relatively higher A_{He} than the SASW. The CH-like SASW shows a large range in proton density and lower alpha particle abundance than the non-CH stream, however both have mean values that fall within the 'intermediate' abundance range (0.015 to 0.045 based on Kasper et al. (2007); Kasper et al. (2012)). This is similar to results for SASW previously
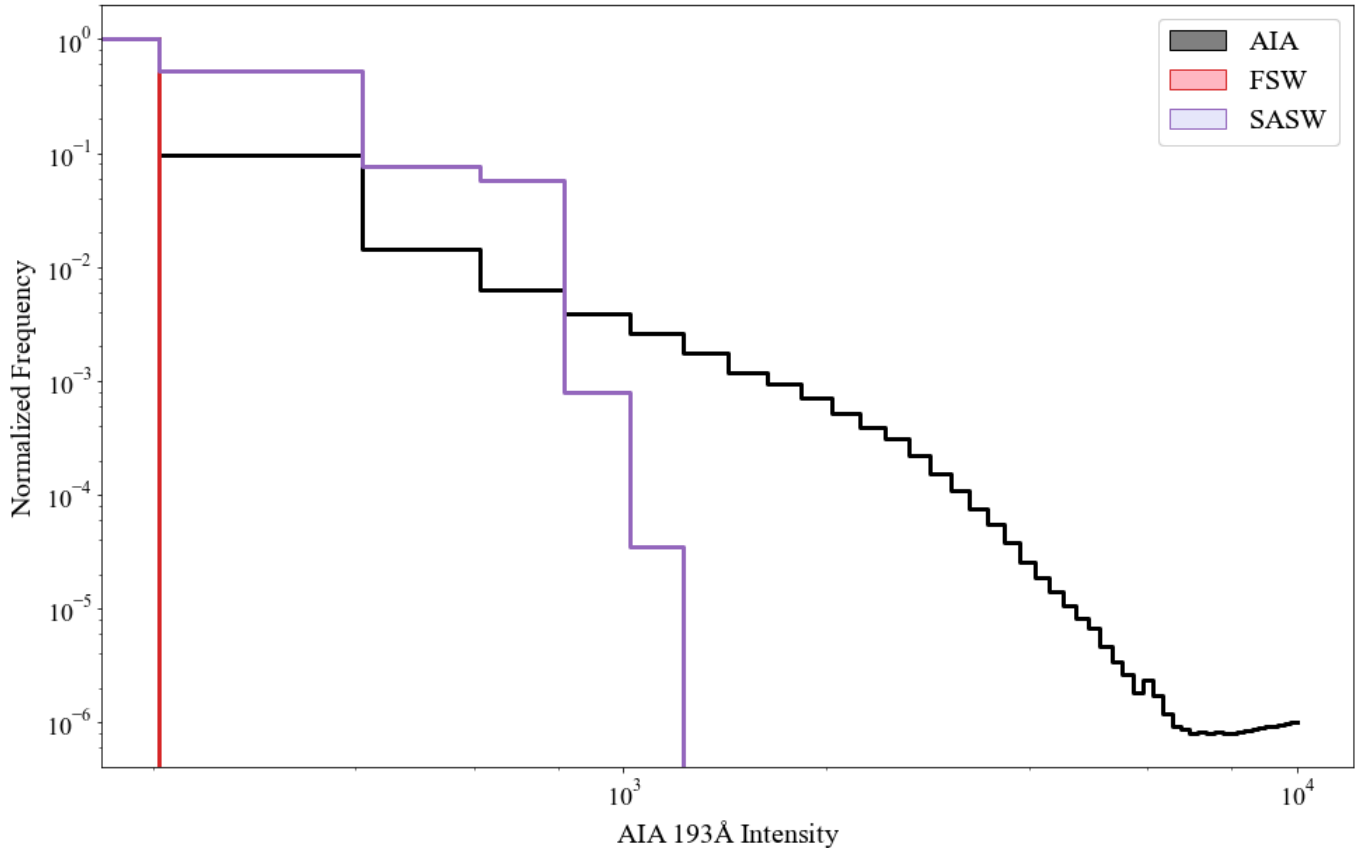
Figure 5. Normalized histograms comparing intensity values from many AIA images with intensity values sampled at the footpoints of the 10 identified and modeled SASW streams. The AIA images chosen are images at a 24-hour cadence for two weeks around each observation.

observed at Parker by Huang et al. (2020); Ervin et al. (2024b); Rivera et al. (2024) and others, contributing to the confusion over source region of the SASW as there is not one abundance level that corresponds to this wind type.

If we assume a frozen-in magnetic field, mass will be conserved along a flux tube allowing for calculation of the proton mass density and energy flux at the coronal base (Wang & Sheeley 2003). The proton mass density n_0v_0 is calculated from the photospheric footpoint field strength determined from the modeling alongside in situ parameters: $n_0v_0 = (B_0/B_r)N_Pv_P$. In Figure 6, we show the calculated proton mass density, and find that the non-CH wind shows dramatically higher mass flux than the CH-like SASW and FSW (similar to the results from Wang & Sheeley (2003)). Higher mass flux is indicative of more heating below the critical point, which is expected to produce wind with slower speeds (Wang et al. 2012).

In Figure 6 Panel (d), we show the normalized differential streaming speed ($\Delta v_{\alpha p}$ / v_A) and see that the FSW streams show much higher differential speeds. Mostafavi et al. (2022) showed correlation between $\Delta v_{\alpha p}$ and v_{sw} and we note that the CH-like SASW has higher differential speeds than the non-CH SASW. This could point to a similar mechanism of preferential acceleration of alpha particles between the FSW and CH-like SASW which would follow from these streams having similar sources.

5. CONCLUSION

Through studying the in situ characteristics and parameters derived from modeling the footpoints of slow Alfvénic wind streams, we find that some (if not many) of these streams originate from coronal holes and their boundary regions. These streams are characterized by high levels of Alfvénicity, slow wind speeds, and intermediate alpha particle abundance in situ. From modeling we find they have weak footpoint field strength (below 10G in most cases),
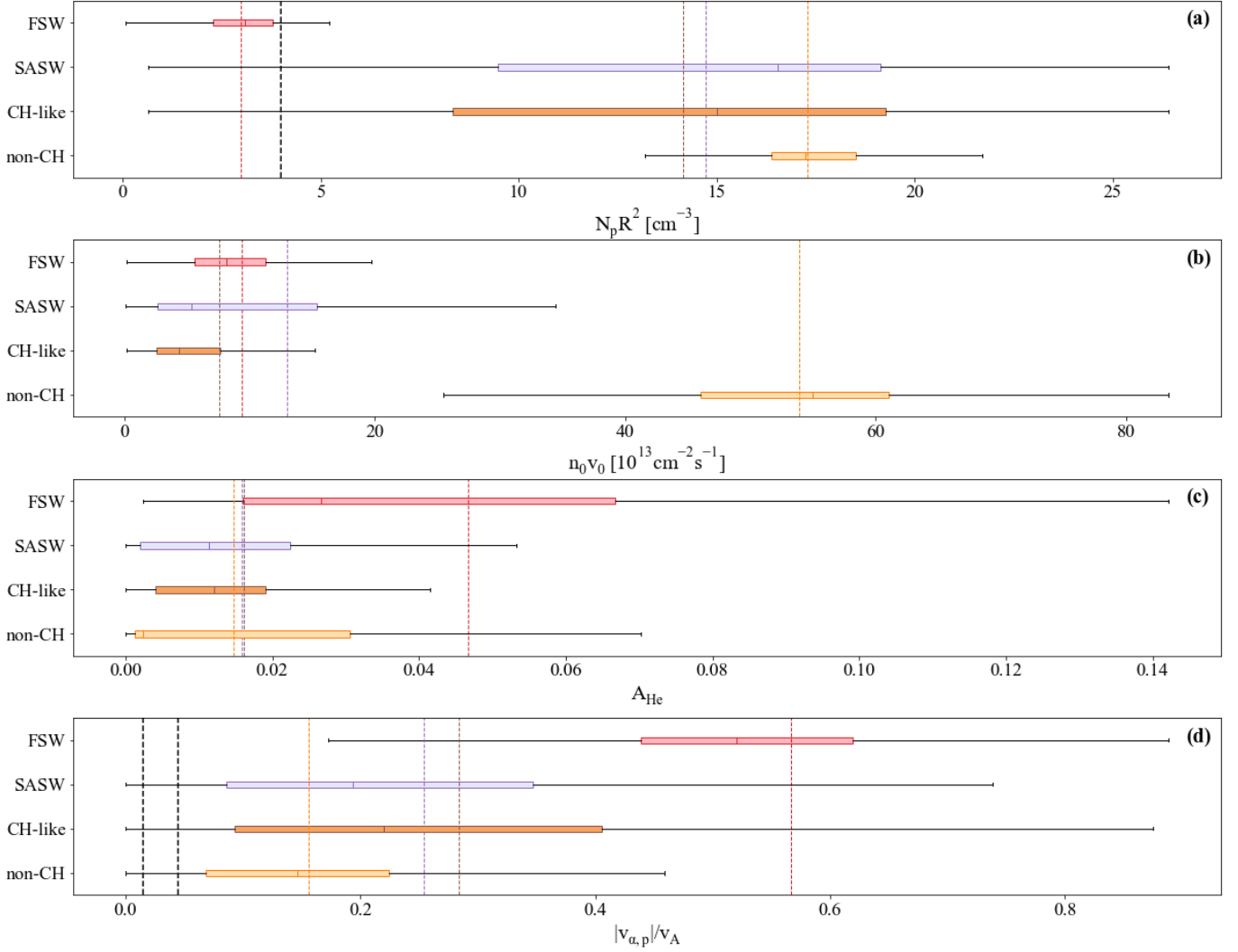
Figure 6. Box plot overviews of compositional parameters for the 10 SASW and 5 FSW streams we modeled. The dashed vertical lines indicate the mean for the distribution with the corresponding color and the solid line shows the median. *Panel (a):* Scaled proton density from SWEAP/SPAN-I. *Panel (b):* Proton mass flux ($n_0 v_0 = (B_0/B_r) N_P v_P$) calculated from in situ observations and the photospheric footpoint field strength from modeling results. *Panel (c):* Alpha abundance ratio (A_{He}) using alpha and proton measurements from SWEAP/SPAN-I. The dashed black lines indicate the high (0.045) and low (0.015) A_{He} thresholds (Kasper et al. 2007; Kasper et al. 2012). *Panel (d):* Normalized differential streaming speed ($\Delta v_{\alpha P} / v_A$).

relatively large expansion factors, and low intensity in EUV (associated with cold temperatures). These streams show higher differential speeds indicating preferential acceleration of alpha particles.

However, we find another class of SASW streams for which identifying the exact source likely requires additional study. These streams show high footpoint field strength (up to 100s G), even larger expansion factors, and high intensity in EUV. Their alpha particle abundance is relatively low and they are associated with incredibly low differential speeds. When compared with EUV observations, these wind streams look to be perhaps emerging from the periphery of active regions or other closed loop structures. These non-CH like streams might emerge from closed loop regions through interchange reconnection, however additional work using composition metrics and other observations is required for conclusive results.

While this work provides an overview of some slow Alfvénic solar wind streams observed by Parker, their modeled sources and associated in situ parameters, there are many caveats that must be considered when coming to conclusions about the true source of the SASW due to the complexity associated with modeling its origins. In this work, we use the

potential field source surface (PFSS) combined with ballistic propagation to estimate the footpoints associated with wind observed in situ by Parker. This modeling method makes huge (potentially unrealistic) assumptions about the magnetic topology of the corona. Additionally, these modeling methods can only trace to sources connected to field lines that are topologically 'open' at the source surface, meaning that connecting to wind from the periphery of closed loops, or streamer blobs is difficult with both aspects likely requiring time dependent modeling. While PFSS can be validated, it is important to remember that these are all 'estimated' footpoints and additional work such as looking at elemental and charge state composition, and comparison with other modeling methods such as magnetohydrodynamic (MHD) models to better capture the more complicated physics in the corona would be useful to have additional confidence in tracing of sources of the slow wind. However, we note that the statistical approach we take here reveals robust trends in source region properties. In particular, it is non-trivial that the properties inferred from modeling and sampling remote observations are systematically distinct when filtering wind of the same speed by cross helicity, an in situ property.

Solar Orbiter, through the Heavy Ion Sensor (HIS; Livi et al. (2023)) will allow us to study the compositional characteristics of the wind in situ and compare with its source region using Spectral Imaging of the Coronal Environment (SPICE; SPICE Consortium et al. (2020)) instrument. Studies using the combination of these instruments, alongside the other remote sensing and in situ instrument aboard Solar Orbiter will support in our understanding of the characteristics associated with wind emerging from various sources, but are likely not enough.

To understand the full scope of the source, formation, evolution, acceleration, and heating mechanisms at work in the solar wind we require multi-point in situ observations at different radial and longitudinal separations with complementary remote sensing observations of the wind's coronal origin. While existing fleets of heliophysics spacecraft including Parker, Solar Orbiter, SDO, Hinode, STEREO, and others provide useful in situ and remote sensing observations of varying wind types, the field still struggles to connect remote and in situ observations because inter-spacecraft coordination is limited and comparing in situ measurements and remote observations of the Sun is difficult. Remote and in situ observations can be better connected through multi-point compositional observations alongside the typical plasma parameters measured throughout the heliosphere that offer a robust method for model validation when connecting the solar wind to its source region at the Sun. Remote observations of solar wind source can provide the coronal temperature, density, outflow speeds, heavy ion composition, and magnetic field properties that can be linked to situ measurements of the solar wind, providing critical constraints to formation and acceleration by interchange reconnection or other mechanisms (Rivera et al. 2022b). Large scale studies using these sorts of observations will allow us to better probe the source regions of the slow wind and understand the acceleration mechanism(s) at work.

APPENDIX

A. VELOCITY CATEGORIZATION

Using observations at 1AU from the Wind 3D Plasma Analyzer (3DP; Lin et al. (1995)) at 1AU, we look at the distribution of velocities over a full solar cycle and for just the time period of interest in this study (January 2020 to December 2022) to look at the fraction of wind at 1AU that is considered classically 'fast'. We are interested in doing this to provide a more quantitative cutoff for solar wind speed to differentiate between fast and slow wind at closer heliocentric distances (see Section 3.1).

Figure 7 shows an overview of the distribution function of solar wind velocity measured by Wind. In panel (a), we show a timeseries of the observations spanning from January 2020 to January 2023 (the time period of Parker Encounters 4 to 14). In panels (b), (c), and (d) we look at the distribution functions over different time periods and the percentage of the wind that falls above the 500km s^{-1} (red) and 400km s^{-1} (blue) thresholds. Panel (b) shows the last 20 years of observations by Wind, we see that a bit over half of the wind is above 400km s^{-1} and $\sim 22\%$ is above 500km s^{-1}. Looking at just the observations during Solar Cycle 24 (Jan 2008 to December 2019), $\sim 20\%$ is above 500km s^{-1} and $\sim 52\%$ is above 400km s^{-1}. Looking at just the period of the Parker observations used in this study (panel (d)), we see that about $\sim 20\%$ of the wind showed speeds above 500 km s^{-1} and $\sim 50\%$ above 400 km s^{-1}. These are the percentage values that we use for our thresholding at described in Section 3.1. Despite some variance in the solar cycle, these thresholds remain consistent over time giving us confidence in these threshold methods.
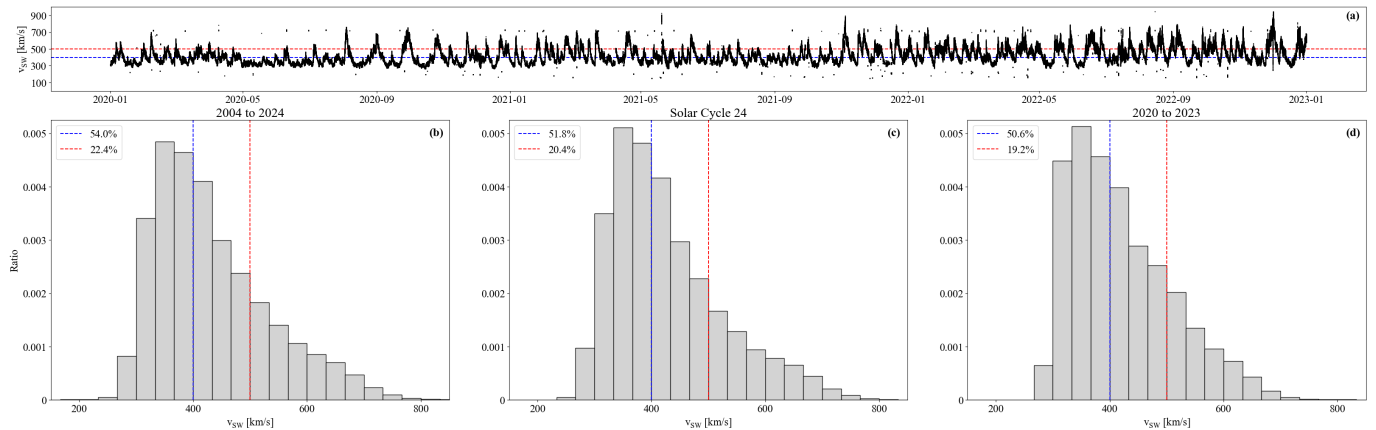
Figure 7. Overview of solar wind velocity observations from the Wind 3DP instrument from 2004 to 2024. *Panel (a):* Time series of solar wind velocity from Wind at 1AU during the time period of this study. *Panel (b):* Distribution of velocity measurements from 2004 to 2024 from Wind. *Panel (c):* Distribution of velocity measurements during Solar Cycle 24 (January 2008 to December 2019). *Panel (d):* Distribution of velocity measurements from 2020 to 2023, covering the time period in this study. In panels (b) to (d), the dashed red and blue lines indicate the 500 km s^{-1} and 400 km s^{-1} speed cutoffs respectively. The legend shows the percentage of observations that fall above that threshold for each period.

B. STREAM OVERVIEWS

In this section, we show an overview of the basic plasma parameters and estimated footpoint mapping from PFSS for the main streams studied in this paper. The AIA images used for comparison with the estimated footpoints are chosen based on an estimation of the emergence time of the stream using ballistic mapping of the Parker trajectory with the measured solar wind speed.

B.1. *Slow Alfvénic Streams*

An overview of the plasma parameters for each of the 10 SASW streams we more closely examined in this study. Each Figure shows the solar wind speed (v_R), absolute cross helicity ($|\sigma_C|$), scaled radial magnetic field ($B_R R^2$), and scaled proton density ($N_P R^2$). The right panel shows a comparison of the estimated footpoints with EUV observations from SDO/AIA.

Figure 8 shows an overview for the SASW stream spanning from 2020-01-28 18:00:00 to 2020-01-29 01:00:00 during Encounter Four. The wind here is seen to emerge from the edge of a coronal at mid-latitudes. The scaled proton density is slightly enhanced over typical 1AU values (5cm^{-3}).
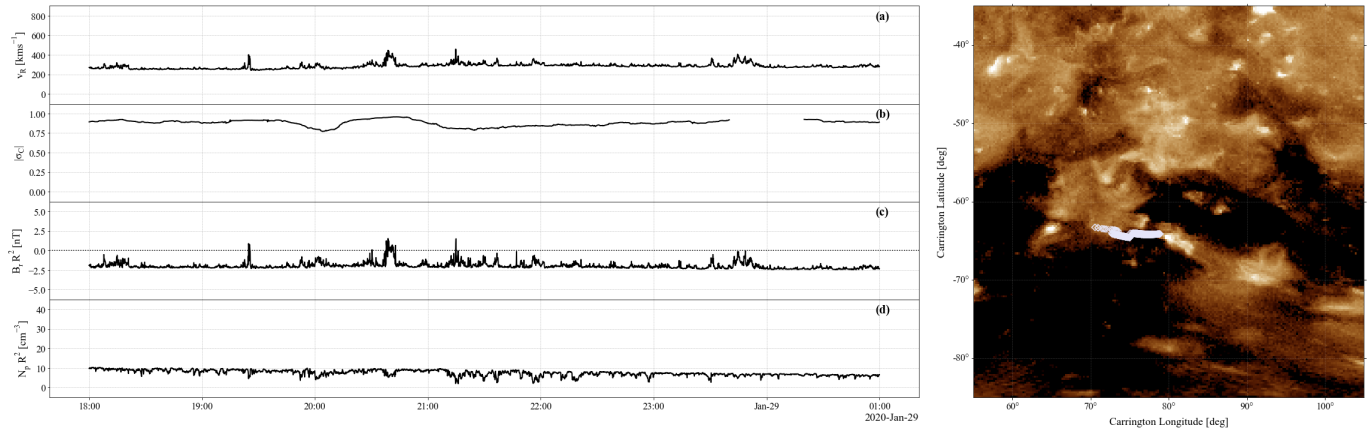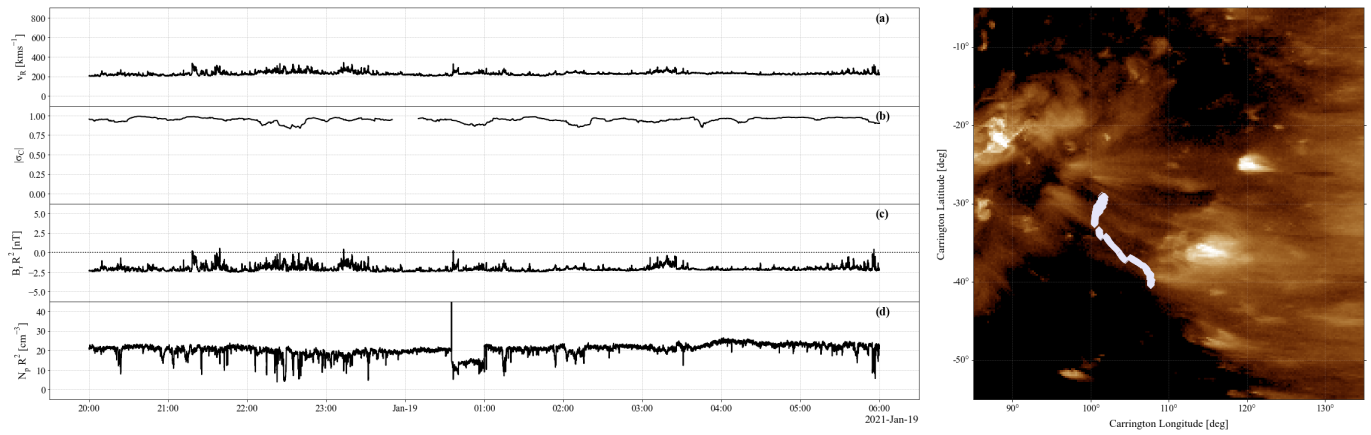

Figure 8. Comparison of in situ characteristics and footpoint estimates for the SASW stream spanning from 2020-01-28 18:00:00 to 2020-01-29 01:00:00 during Encounter Four.

Figure 9 shows an overview for the SASW stream spanning from 2020-06-06 06:00:00 to 2020-06-06 09:00:00 during Encounter Five. The wind here is emerges from a CH edge / small mid-latitude CH. The scaled proton density is slightly enhanced over typical 1AU values (5cm^{-3}).
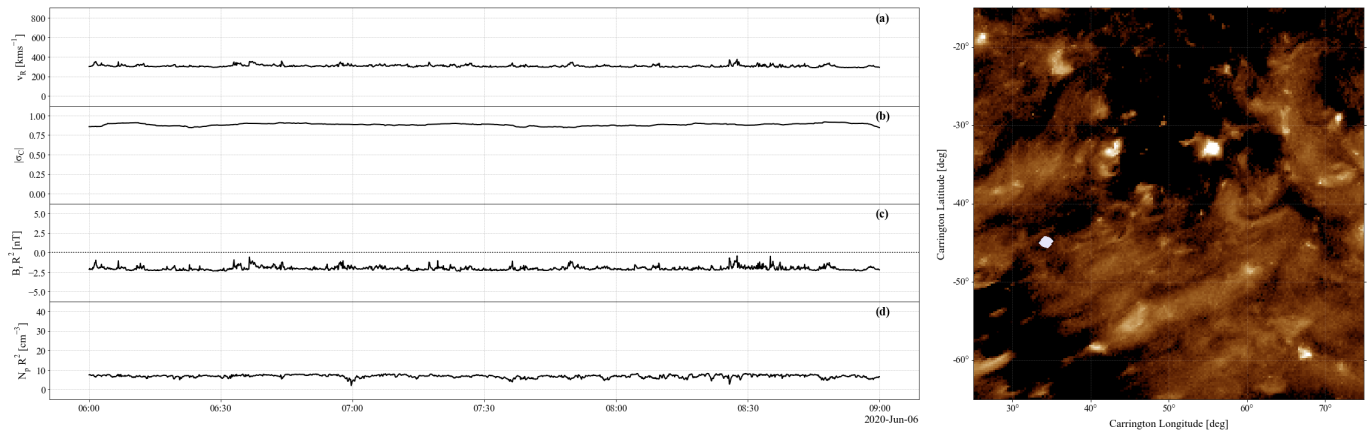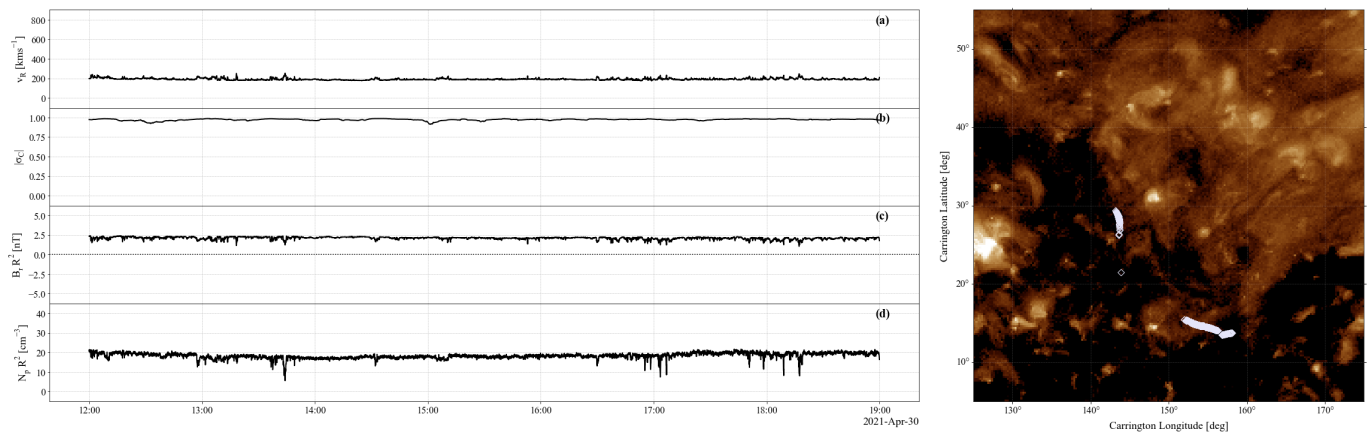

Figure 9. Comparison of in situ characteristics and footpoint estimates for the SASW stream spanning from 2020-06-06 06:00:00 to 2020-06-06 09:00:00 during Encounter Five.

Figure 10 shows an overview for the SASW stream spanning from 2020-06-09 10:00:00 to 2020-06-09 22:00:00 during Encounter Five. The wind here is seen to emerge from a small, mid-latitude CH. The scaled proton density is enhanced over typical 1AU values (5cm^{-3}).
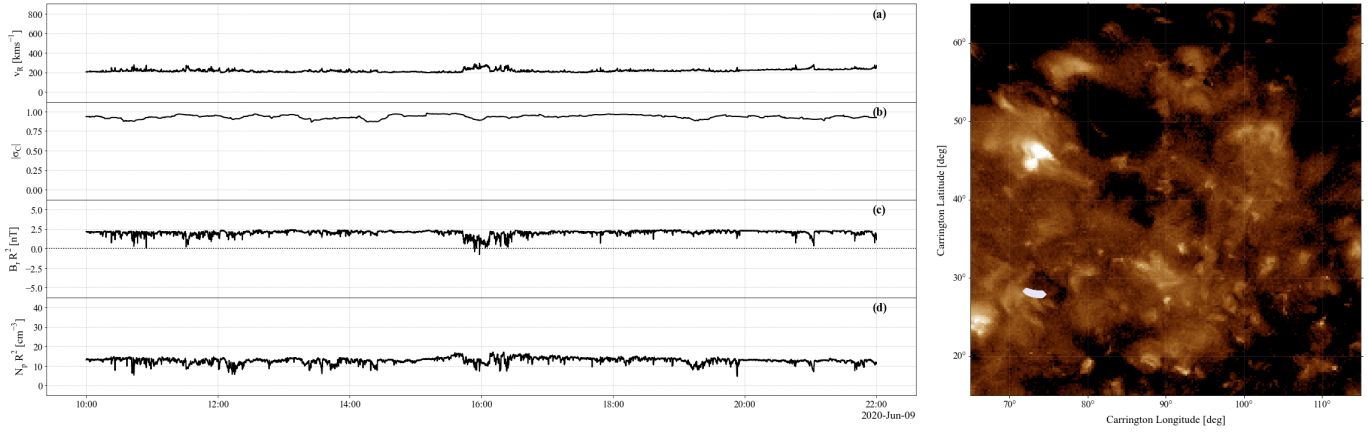
Figure 10. Comparison of in situ characteristics and footpoint estimates for the SASW stream spanning from 2020-06-09 10:00:00 to 2020-06-09 22:00:00 during Encounter Five.

Figure 11 shows an overview for the SASW stream spanning from 2020-09-27 12:00:00 to 2020-09-27 16:00:00 during Encounter Six. The wind here is seen to emerge from the edge of a coronal at mid-latitudes. The scaled proton density is slightly enhanced over typical 1AU values (5cm^{-3}).
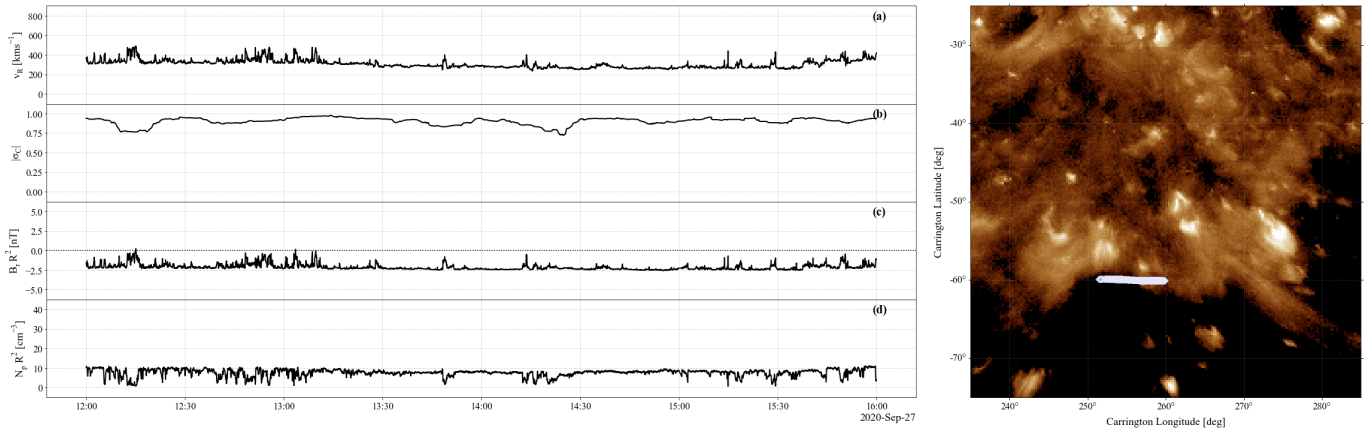
Figure 11. Comparison of in situ characteristics and footpoint estimates for the SASW stream spanning from 2020-09-27 12:00:00 to 2020-09-27 16:00:00 during Encounter Six.

Figure 12 shows an overview for the SASW stream spanning from 2021-01-18 18:00:00 to 2021-01-19 06:00:00 during Encounter Seven. The wind here is seen to emerge from the edge of a coronal at mid-latitudes, with the footpoints outlining the edge of an observed CH. The scaled proton density is enhanced over typical 1AU values (5cm^{-3}).

Figure 13 shows an overview for the SASW stream spanning from 2021-04-30 00:00:00 to 2021-04-30 05:00:00 during Encounter Eight. This wind stream is very smooth and seems to emerge from the periphery of an active region, with an incredibly incompressible magnetic field, smooth wind speed and enhanced proton density.

Figure 14 shows an overview for the SASW stream spanning from 2021-04-30 10:00:00 to 2021-05-01 00:00:00 during Encounter Eight. This wind streams emerges from the peripheries of a coronal hole and shows enhanced proton density.

Figure 15 shows an overview for the SASW stream spanning from 2022-12-10 18:00:00 to 2022-12-10 19:00:00 during Encounter Fourteen. This wind streams shows a large amount of structure, indicative of non-CH wind. It seems to emerge from the edges of a loop like structure at active latitudes and shows structure and enhancement in the proton density.
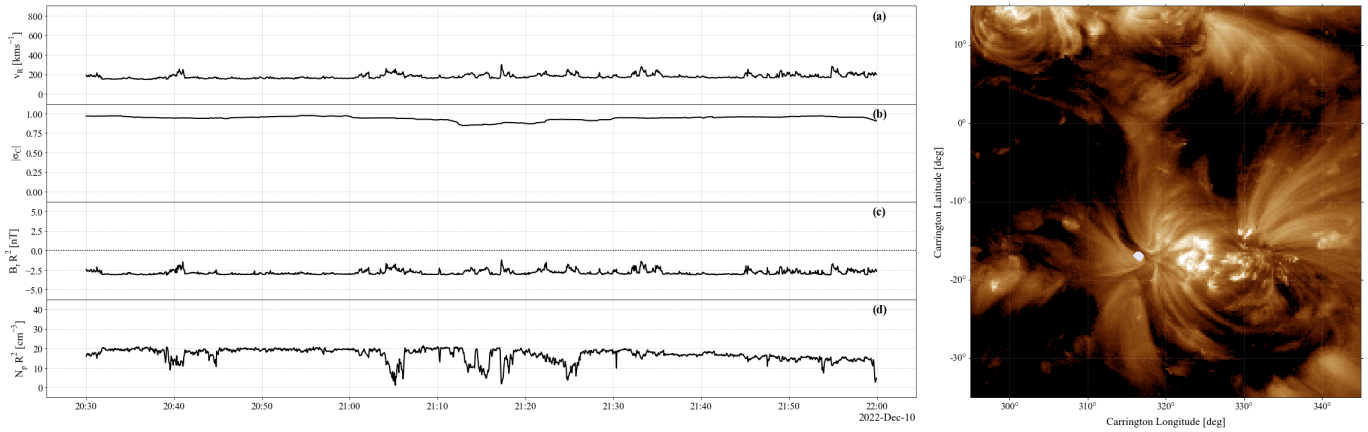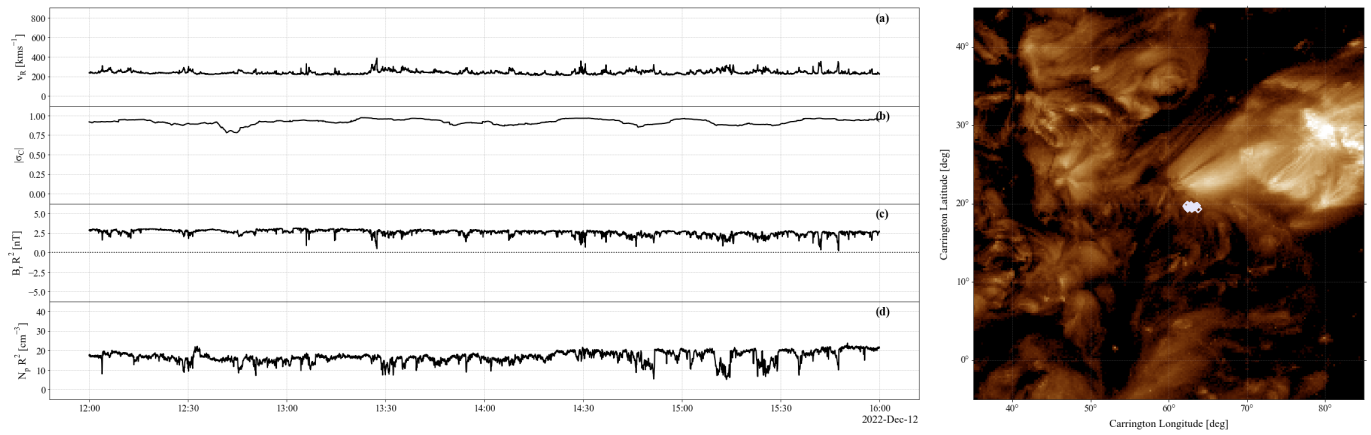
Figure 12. Comparison of in situ characteristics and footpoint estimates for the SASW stream spanning from 2021-01-18 18:00:00 to 2021-01-19 06:00:00 during Encounter Seven.
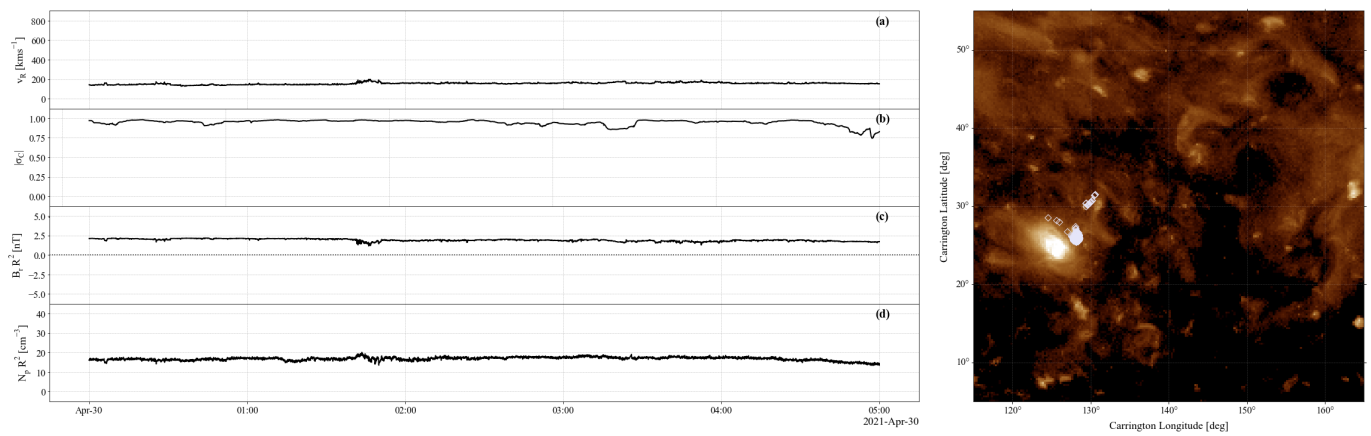
Figure 13. Comparison of in situ characteristics and footpoint estimates for the SASW stream spanning from 2021-04-30 00:00:00 to 2021-04-30 05:00:00 during Encounter Eight.

Figure 14. Comparison of in situ characteristics and footpoint estimates for the SASW stream spanning from 2021-04-30 10:00:00 to 2021-05-01 00:00:00 during Encounter Eight.
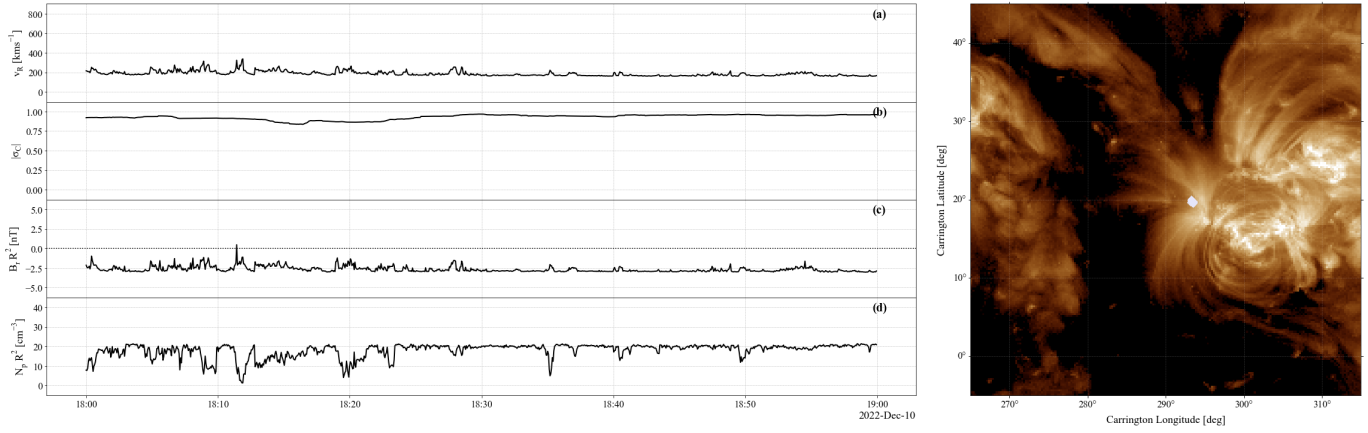
Figure 15. Comparison of in situ characteristics and footpoint estimates for the SASW stream spanning from 2022-12-10 18:00:00 to 2022-12-10 19:00:00 during Encounter Fourteen.
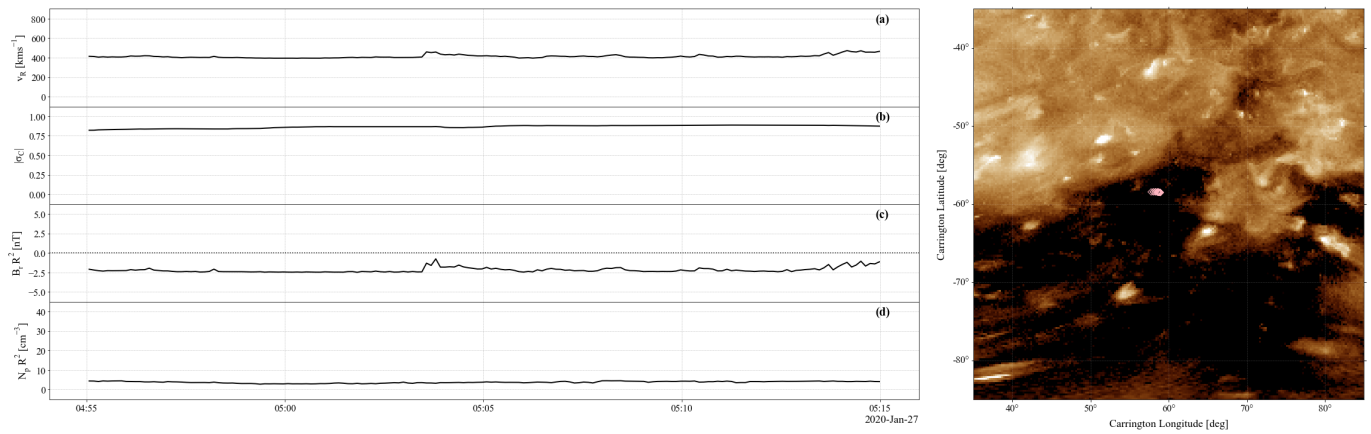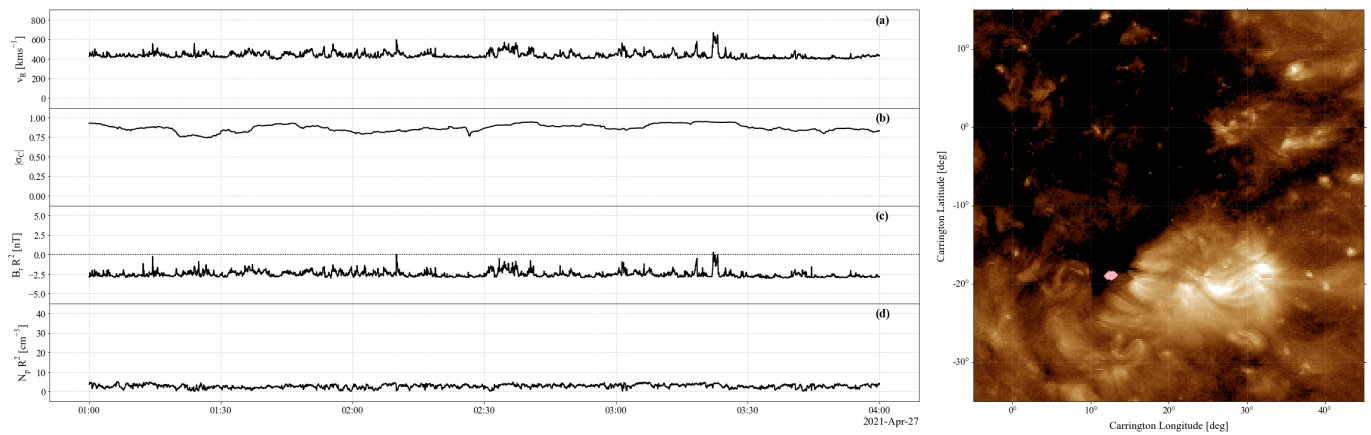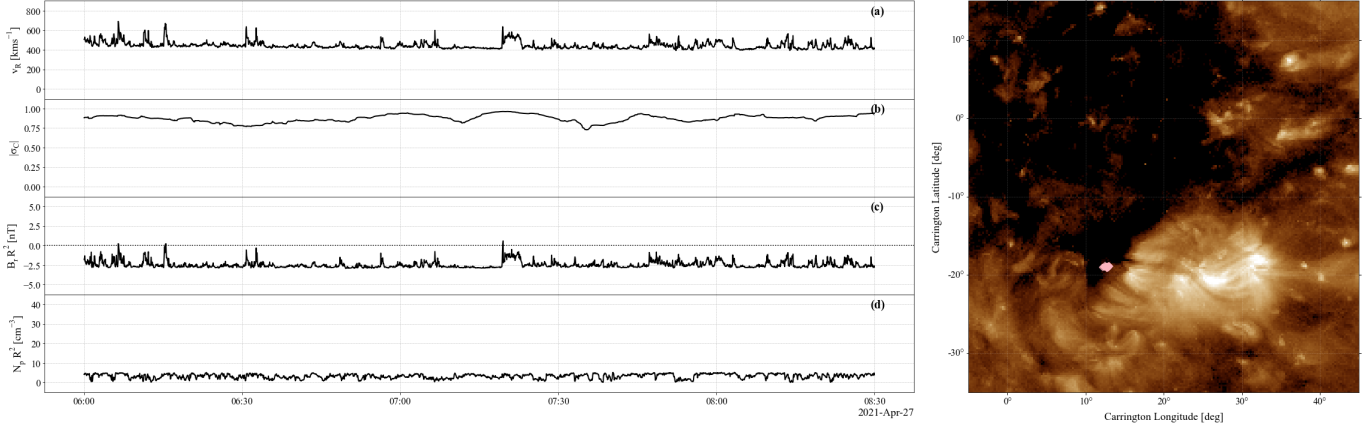
Figure 16 for the SASW stream spanning from 2022-12-10 20:30:00 to 2022-12-10 22:00:00 during Encounter Fourteen. This wind streams shows a large amount of structure, indicative of non-CH wind. It seems to emerge from the edges of a loop like structure at active latitudes and shows structure and enhancement in the proton density.

Figure 16. Comparison of in situ characteristics and footpoint estimates for the SASW stream spanning from 2022-12-10 20:30:00 to 2022-12-10 22:00:00 during Encounter Fourteen.

Figure 17 shows an overview for the SASW stream spanning from 2022-12-12 12:00:00 to 2022-12-12 16:00:00 during Encounter Fourteen. This wind streams shows enhanced proton density and looks to emerge from the periphery of a coronal hole near an active region structure. There is structure in the velocity, magnetic field, and observed proton density.

B.2. *Fast Wind Streams*

An overview of the plasma parameters and footpoint mapping for the 5 FSW streams modeled for this study. These five streams all emerge from within or near the boundaries of coronal hole structures.

Figure 18 shows an overview for the SASW stream spanning from 2020-01-27 04:55:00 to 2020-01-27 05:15:00 during Encounter Four.

Figure 19 shows an overview for the SASW stream spanning from 2021-04-27 01:00:00 to 2021-04-27 04:00:00 during Encounter Eight.

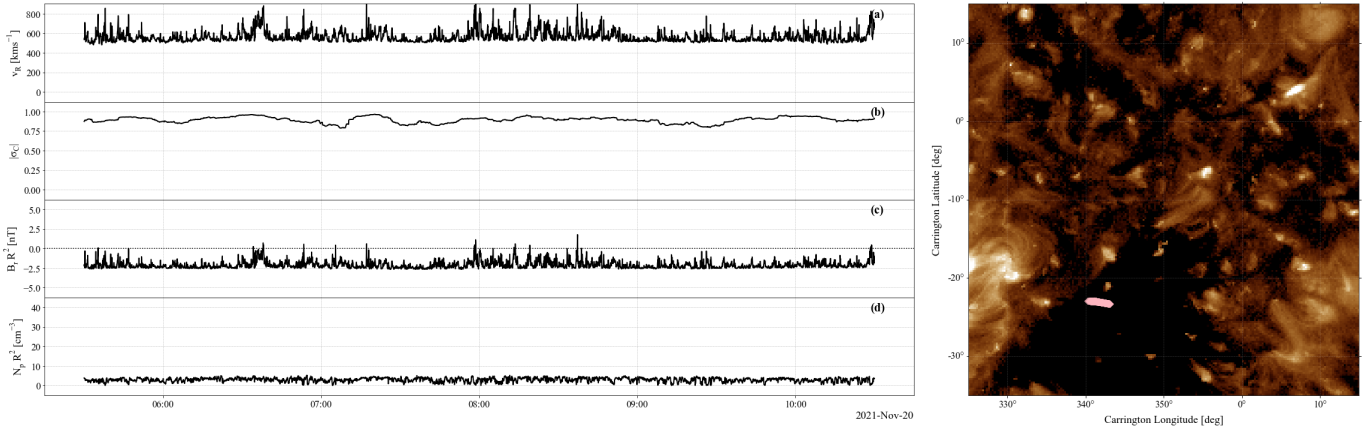Figure 20 shows an overview for the SASW stream spanning from 2021-04-27 06:00:00 to 2021-04-27 08:30:00 during Encounter Eight.

Figure 17. Comparison of in situ characteristics and footpoint estimates for the SASW stream spanning from 2022-12-12 12:00:00 to 2022-12-12 16:00:00 during Encounter Fourteen.

Figure 18. Comparison of in situ characteristics and footpoint estimates for the FSW stream spanning from 2020-01-27 04:55:00 to 2020-01-27 05:15:00 during Encounter Four.

Figure 19. Comparison of in situ characteristics and footpoint estimates for the FSW stream spanning from 2021-04-27 01:00:00 to 2021-04-27 04:00:00 during Encounter Eight.
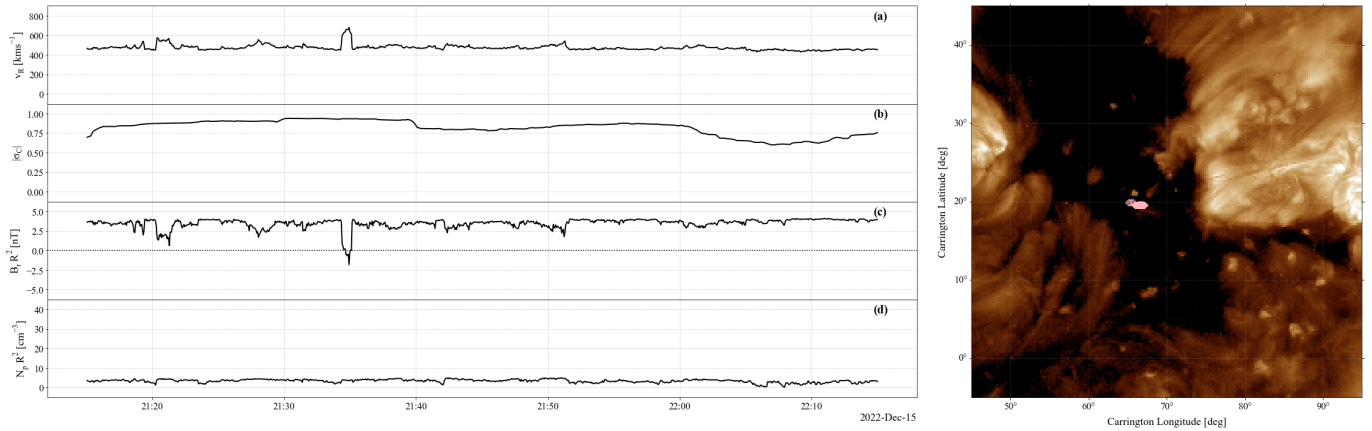
Figure 20. Comparison of in situ characteristics and footpoint estimates for the FSW stream spanning from 2021-04-27 06:00:00 to 2021-04-27 08:30:00 during Encounter Eight.

Figure 21 shows an overview for the SASW stream spanning from 2021-11-20 05:30:00 to 2021-11-20 10:30:00 during Encounter Ten.

Figure 21. Comparison of in situ characteristics and footpoint estimates for the FSW stream spanning from 2021-11-20 05:30:00 to 2021-11-20 10:30:00 during Encounter Ten.

Figure 22 shows an overview for the SASW stream spanning from 2022-12-15 21:15:00 to 2022-12-15 22:15:00 during Encounter Fourteen. This stream comes from the center of a coronal hole and has scaled proton densities $\sim 5\mathrm{cm}^{-3}$.

C. MODEL VALIDATION

This study uses the Potential Field Source Surface (PFSS) model alongside ballistic propagation methods to estimate the footpoints of plasma streams of interest. The PFSS model has two inputs that can lead to variance in the overall results: the choice of input magnetogram and source surface height. Similar to methods previously outlined in Badman et al. (2020, 2022); Ervin et al. (2024b); Ervin et al. (2024) we look at the effect of these two parameters to understand the impact on our conclusions.

The ballistic propagation results depend on the in situ v_R measurement and methodology, and the results of this projection can impact the estimated footpoints. We probe how variance in the input velocity effect our footpoint estimations (Ervin et al. 2024b; Ervin et al. 2024). We vary the inputted in situ v_R used to calculate the source surface trajectory via ballistic propagation by bootstrapping noise on at a level of 4% – the estimated systematic uncertainty in the SPAN-I velocity moment (3%) plus some extra noise to account for random sources of error (Livi et al. 2022). From these new source surface trajectories, we calculate the estimated footpoint from PFSS with the

Figure 22. Comparison of in situ characteristics and footpoint estimates for the FSW stream spanning from 2022-12-15 21:15:00 to 2022-12-15 22:15:00 during Encounter Fourteen.

'best' magnetogram used for identifying the source region of each SASW and FSW stream. There are a variety of source of noise and uncertainty in the SPAN-I velocity measurements and this methodology aims to show how noise and uncertainty in the velocity measurement affect the resulting source surface trajectory and footpoints.

In Figure 23, we show an overview of the variance in the source surface trajectory when adding noise of 4% to the in situ v_R. We choose three streams to represent different characteristics speeds: fast, slow, and slower, and show how the slower wind speeds are more affected by the inputted velocity to the ballistic propagation. This is one contributing factor to the difficulty in determining the sources of the slow wind in comparison to the source of faster streams. Figure 23 shows how the uncertainty in the velocity translates to 'error' on the estimated footpoints determined from PFSS. In the top row we show the distribution of error on our estimated footpoints finding it to be less than $1°$ for these periods. In panels (d) to (f) we show how the error in ballistic propagation impacts the resulting source surface trajectory and finally the footpoint estimation (panels (g) to (i)).

We see that while the exact coordinate position in terms of longitude/latitude has some slight variance (see panels (a) to (c) and (g) to (i)), the overall source region remains unaffected. There is an obvious correlation between the speed of the wind stream and the effects on ballistic propagation, notably that there is more error in slow wind streams than in fast, a contributor to the issues surrounding modeling the true source of slow wind. Dakeyo et al. (2024) found similar results noting that the estimated error was $\leq 5°$ and that the error decreased with heliocentric distance and had an inverse correlation with wind speed.

In the PFSS model, the chosen source surface height can impact the outputted footpoints as this height (R_{ss}) determines that point at which the field is forced to be purely radial. For each of the streams of interest, we vary the height of the source surface between 2.0 $R_\odot$ and 3.5 $R_\odot$ to understand how this impacts the resulting footpoints. We see in Figure 24 that changing the source surface height leads to large variance in the location of the footpoints, we see from Figure 25 that the optimal R_{ss} is 2.5$R_\odot$. Varying R_{ss} impacts the exact position of the footpoint (especially in latitude), however it does not impact the resulting source region. It does have a larger effect on the resulting footpoints in comparison with the effect of the error of the in situ v_R measurement. We use a source surface height of 2.5 $R_\odot$ for our modeling as this produces the best result in terms of matching the modeled polarity with the measured magnetic field polarity from FIELDS. Similar to the error in the ballistic propagation, we see that this most impacts slower wind streams.

The last user input to PFSS, the choice of input magnetogram, also impacts the resulting footpoint. We choose a 'best' magnetogram by comparing the outputted polarity from the PFSS model to the observed polarity by Parker and optimizing such that the neutral line crossings match. To quantify the impact on the estimated footpoints by this choice, we use magnetograms from ± 2 days around our choice of magnetograms with a R_{ss} of 2.5 $R_\odot$ and compare results. We find that this produces an error on the estimated footpoint of $\sim 2°$ and thus is an important consideration when validating the PFSS model.

Through this analysis of the ballistic propagation and PFSS processes required to trace from the spacecraft down to estimated photospheric footpoints, we see that there are a variety of error sources which can impact the results. Most
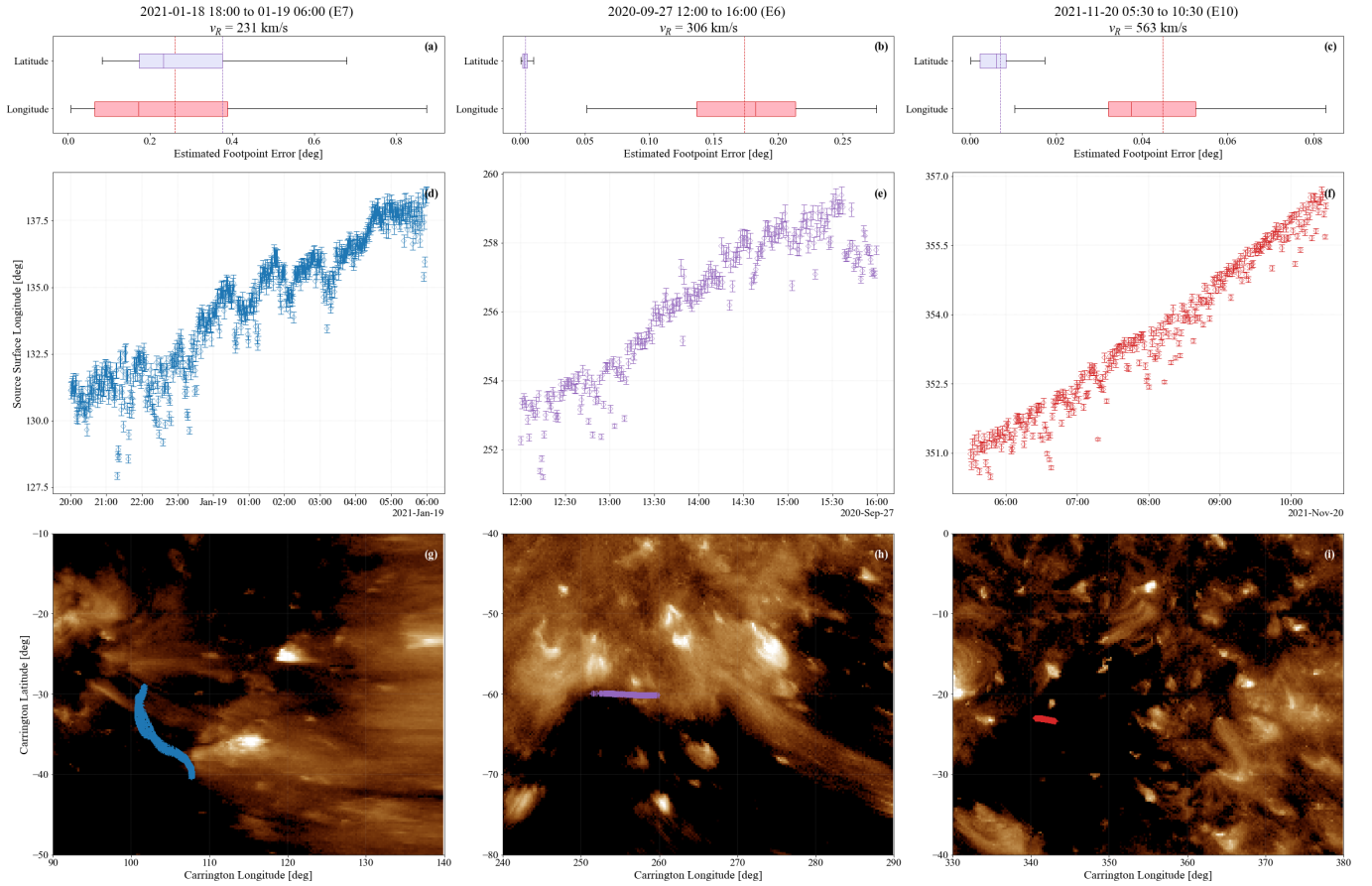
Figure 23. Overview of error on estimated PFSS footpoints due to noise in the velocity measurement used for ballistic propagation. We use three streams of different speeds to show how the effect varies based on v_{sw}. The top row (panels (a), (b), (c)) show the overall error on the latitude and longitude of the footpoints. The middle row (panels (d), (e), (f)) show the error on the source surface longitude as a function of time. The bottom row (panels (g) to (i)) shows the error on the footpoints compared with the associated AIA image.

notably, the source surface height has the largest impact on the resulting footpoints. Much work has been done looking at this height, comparing it with other models, optimizing to reproduce the observed open flux, and considering a non-spherical source surface to better reproduce observations. We see that the impact of the errors in the ballistic propagation and PFSS are considerably less impactful for the fast wind, further contributing to the difficulties in determining the source of the slow wind. While we can validate our models with magnetic field observations, multi point observations would provide additional measurements for further constraints and confidence in our results. In this work, we look at statistical distributions of parameters and while overlaps in distributions could be attributable to the error sources described above, it would not the systematic shift in source region properties seen in Figure 4. This indicates that the observed differences are real and due to variance source regions of the wind.

REFERENCES

Alterman, B. L., & Kasper, J. C. 2019, The Astrophysical Journal Letters, 879, L6, doi: 10.3847/2041-8213/ab2391

Alterman, B. L., Kasper, J. C., Stevens, M. L., & Koval, A. 2018, ApJ, 864, 112, doi: 10.3847/1538-4357/aad23f

Altschuler, M. D., & Newkirk, G. 1969, SoPh, 9, 131, doi: 10.1007/BF00145734

Angelopoulos, V., Cruce, P., Drozdov, A., et al. 2019, Space Science Reviews, 215, 9, doi: 10.1007/s11214-018-0576-4

Annex, A., Pearson, B., Seignovert, B., et al. 2020, The Journal of Open Source Software, 5, 2050, doi: 10.21105/joss.02050
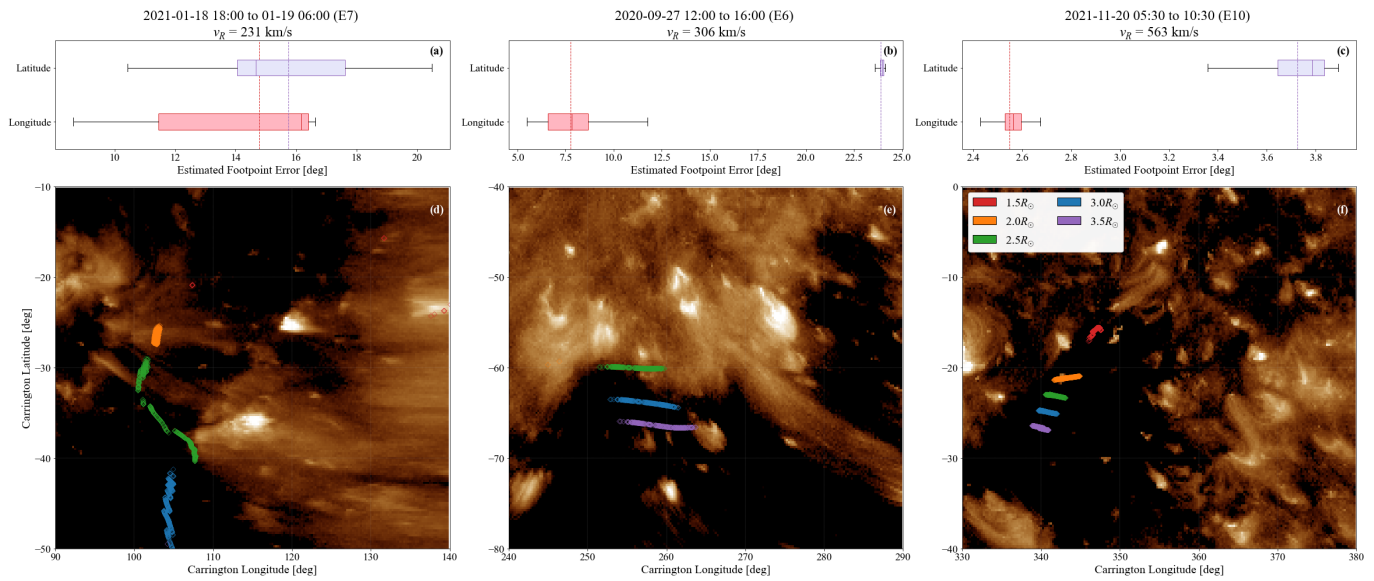
Figure 24. Comparison of the error on the estimated footpoints due to changing the source surface height for streams of varying speeds. Panels (a) to (c) show the overall error on the footpoints as a box plot. Panels (d) to (f) show the footpoints associated with different source surface heights on the associated AIA image.

Arge, C. N., Henney, C. J., Hernandez, I. G., et al. 2013, in American Institute of Physics Conference Series, Vol. 1539, Solar Wind 13, ed. G. P. Zank, J. Borovsky, R. Bruno, J. Cirtain, S. Cranmer, H. Elliott, J. Giacalone, W. Gonzalez, G. Li, E. Marsch, E. Moebius, N. Pogorelov, J. Spann, & O. Verkhoglyadova, 11–14, doi: 10.1063/1.4810977

Arge, C. N., Henney, C. J., Koller, J., et al. 2010, in American Institute of Physics Conference Series, Vol. 1216, Twelfth International Solar Wind Conference, ed. M. Maksimovic, K. Issautier, N. Meyer-Vernet, M. Moncuquet, & F. Pantellini, 343–346, doi: 10.1063/1.3395870

Arge, C. N., Henney, C. J., Koller, J., et al. 2011, in Astronomical Society of the Pacific Conference Series, Vol. 444, 5th International Conference of Numerical Modeling of Space Plasma Flows (ASTRONUM 2010), ed. N. V. Pogorelov, E. Audit, & G. P. Zank, 99

Arge, C. N., Luhmann, J. G., Odstrcil, D., Schrijver, C. J., & Li, Y. 2004, Journal of Atmospheric and Solar-Terrestrial Physics, 66, 1295, doi: 10.1016/j.jastp.2004.03.018

Arge, C. N., Odstrcil, D., Pizzo, V. J., & Mayer, L. R. 2003, AIP Conference Proceedings, 679, 190, doi: 10.1063/1.1618574

Arge, C. N., & Pizzo, V. J. 2000, J. Geophys. Res., 105, 10465, doi: 10.1029/1999JA000262

Asplund, M., Amarsi, A. M., & Grevesse, N. 2021, A&A, 653, A141, doi: 10.1051/0004-6361/202140445

Astropy Collaboration, Robitaille, T. P., Tollerud, E. J., et al. 2013, A&A, 558, A33, doi: 10.1051/0004-6361/201322068

Astropy Collaboration, Price-Whelan, A. M., Sipőcz, B. M., et al. 2018, AJ, 156, 123, doi: 10.3847/1538-3881/aabc4f

Astropy Collaboration, Price-Whelan, A. M., Lim, P. L., et al. 2022, ApJ, 935, 167, doi: 10.3847/1538-4357/ac7c74

Badman, S. T., Bale, S. D., Martínez Oliveros, J. C., et al. 2020, ApJS, 246, 23, doi: 10.3847/1538-4365/ab4da7

Badman, S. T., Brooks, D. H., Poirier, N., et al. 2022, ApJ, 932, 135, doi: 10.3847/1538-4357/ac6610

Bale, S. D., Goetz, K., Harvey, P. R., et al. 2016, SSRv, 204, 49, doi: 10.1007/s11214-016-0244-5

Bavassano, B., Pietropaolo, E., & Bruno, R. 1998, J. Geophys. Res., 103, 6521, doi: 10.1029/97JA03029

Boldyrev, S. 2006, Phys. Rev. Lett., 96, 115002, doi: 10.1103/PhysRevLett.96.115002

Buergi, A., & Geiss, J. 1986, SoPh, 103, 347, doi: 10.1007/BF00147835

Chandran, B. D. G., Schekochihin, A. A., & Mallet, A. 2015, ApJ, 807, 39, doi: 10.1088/0004-637X/807/1/39

Chen, C. H. K., Bale, S. D., Bonnell, J. W., et al. 2020, ApJS, 246, 53, doi: 10.3847/1538-4365/ab60a3

Chen, Y., Esser, R., & Hu, Y. 2003, ApJ, 582, 467, doi: 10.1086/344642

Clark, R., Harvey, J., Hill, F., & Toner, C. 2003, in AAS/Solar Physics Division Meeting, Vol. 34, AAS/Solar Physics Division Meeting #34, 08.03
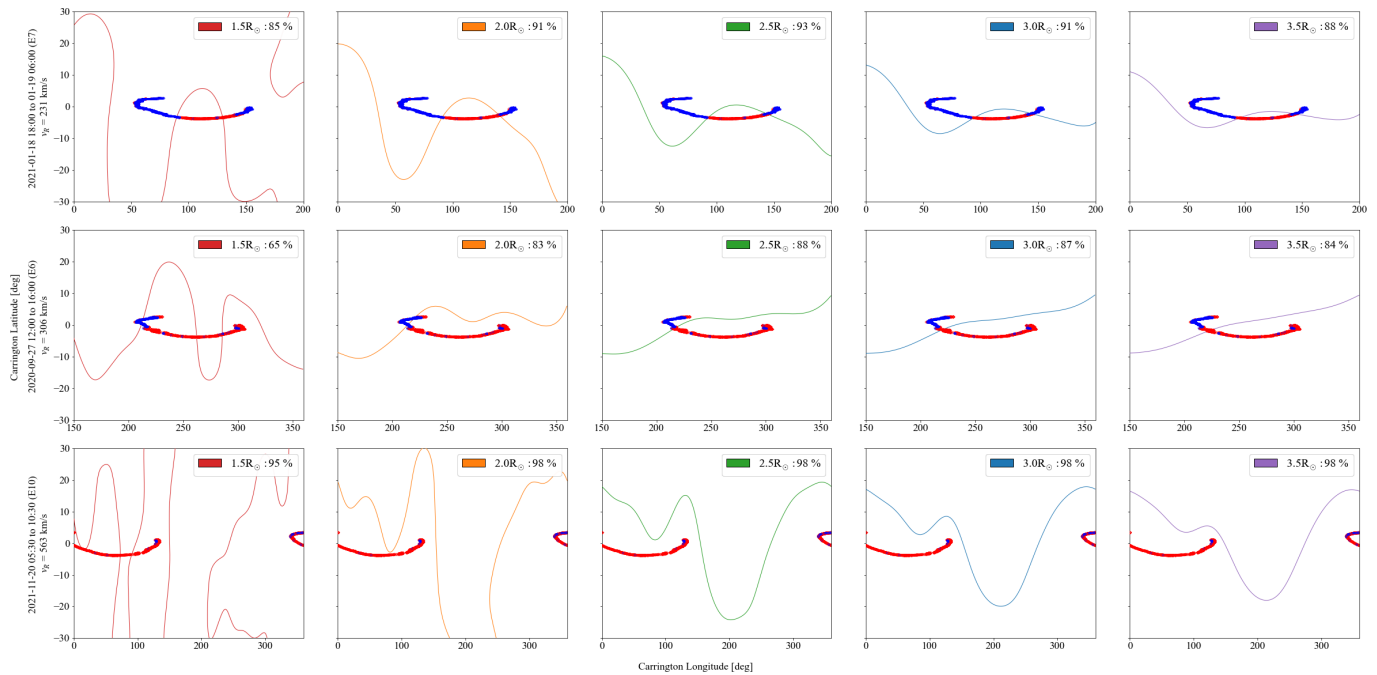
Figure 25. Validation of our choice of source surface height (R_{ss}) for the three different streams we have discussed in this section. The rows corresponding to the streams from E7, E6, and E10 from top to bottom respectively. The trajectory of Parker at the source surface is shown in blue (negative polarity) and red (positive polarity) based on the measurements from Parker/FIELDS. The heliospheric current sheet from the PFSS model is compared with the trajectory and we show the percentage of correct polarity the model predicted in the legend.

Community, T. S., Barnes, W. T., Bobra, M. G., et al.
2020, The Astrophysical Journal, 890, 68,
doi: 10.3847/1538-4357/ab4f7a

Cranmer, S. R. 2009, Living Reviews in Solar Physics, 6, 3,
doi: 10.12942/lrsp-2009-3

Dakeyo, J. B., Badman, S. T., Rouillard, A. P., et al. 2024,
A&A, 686, A12, doi: 10.1051/0004-6361/202348892

D'Amicis, R., & Bruno, R. 2015, ApJ, 805, 84,
doi: 10.1088/0004-637X/805/1/84

D'Amicis, R., Matteini, L., & Bruno, R. 2018, Monthly
Notices of the Royal Astronomical Society, 483, 4665,
doi: 10.1093/mnras/sty3329

D'Amicis, R., Perrone, D., Bruno, R., & Velli, M. 2021,
Journal of Geophysical Research: Space Physics, 126,
e2020JA028996,
doi: https://doi.org/10.1029/2020JA028996

Ervin, T., Jaffarove, K., Badman, S., et al. 2024a, Code to
reproduce figures for Ervin et al. (2024c): Characteristics
and Source Regions of Slow Alfv enic Solar Wind
Observed by Parker Solar Probe., v1, Zenodo,
doi: 10.5281/zenodo.12734997

Ervin, T., Bale, S. D., Badman, S. T., et al. 2024b,
Compositional metrics of fast and slow Alfvenic solar
wind emerging from coronal holes and their boundaries.
https://arxiv.org/abs/2309.07949

Ervin, T., Bale, S. D., Badman, S. T., et al. 2024, arXiv
e-prints, arXiv:2405.15844,
doi: 10.48550/arXiv.2405.15844

Feldman, U., Landi, E., & Laming, J. M. 2005, ApJ, 619,
1142, doi: 10.1086/426539

Feldman, W. C., & Marsch, E. 1997, in Cosmic Winds and
the Heliosphere, 617

Fisk, L. A. 2003, Journal of Geophysical Research (Space
Physics), 108, 1157, doi: 10.1029/2002JA009284

Garton, T. M., Murray, S. A., & Gallagher, P. T. 2018, The
Astrophysical Journal Letters, 869, L12,
doi: 10.3847/2041-8213/aaf39a

Geiss, J., Gloeckler, G., & Von Steiger, R. 1995, Space
Science Reviews, 72, 49, doi: 10.1007/BF00768753

Goldreich, P., & Sridhar, S. 1995, \apj, 438, 763,
doi: 10.1086/175121

—. 1997, \apj, 485, 680, doi: 10.1086/304442

Harris, C. R., Millman, K. J., van der Walt, S. J., et al.
2020, Nature, 585, 357, doi: 10.1038/s41586-020-2649-2

Harvey, J. W., Hill, F., Hubbard, R. P., et al. 1996,
Science, 272, 1284, doi: 10.1126/science.272.5266.1284

Hickmann, K. S., Godinez, H. C., Henney, C. J., & Arge,
C. N. 2015, Solar Physics, 290, 1105,
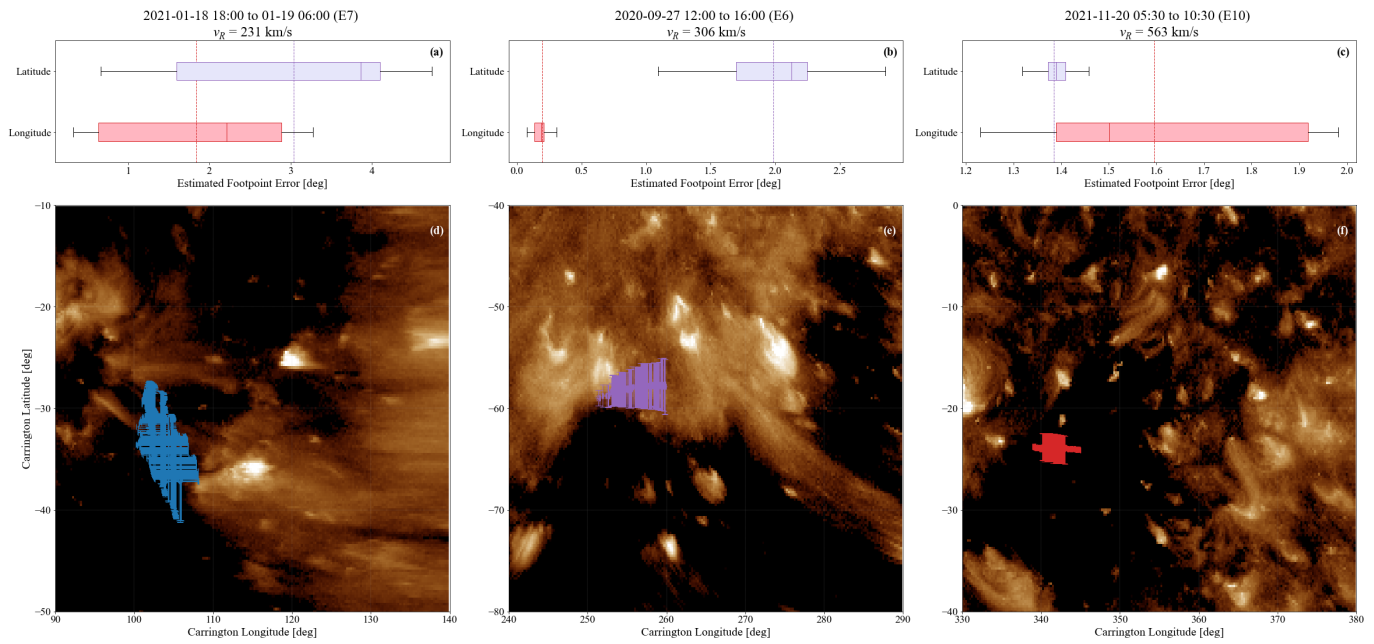doi: 10.1007/s11207-015-0666-3

Figure 26. Comparison of the effect of the choice of input magnetogram for the lower PFSS boundary condition on the estimated footpoints for streams of varied speeds. Panels (a) to (c) show the overall error on the estimated footpoint for each of the wind streams of interest. Panels (d) to (f) show the footpoints and their error on the associated AIA images.

Hoeksema, J. T. 1984, PhD thesis, Stanford University, California

Huang, J., Kasper, J. C., Stevens, M., et al. 2020, arXiv e-prints, arXiv:2005.12372, doi: 10.48550/arXiv.2005.12372

Hunter, J. D. 2007, Computing in Science & Engineering, 9, 90, doi: 10.1109/MCSE.2007.55

Johnson, M., Rivera, Y. J., Niembro, T., et al. 2024, ApJ, 964, 81, doi: 10.3847/1538-4357/ad2510

Kasper, J. C., Stevens, M. L., Korreck, K. E., et al. 2012, The Astrophysical Journal, 745, 162, doi: 10.1088/0004-637X/745/2/162

Kasper, J. C., Stevens, M. L., Lazarus, A. J., Steinberg, J. T., & Ogilvie, K. W. 2007, ApJ, 660, 901, doi: 10.1086/510842

Kasper, J. C., Abiad, R., Austin, G., et al. 2016, Space Science Reviews, 204, 131, doi: 10.1007/s11214-015-0206-3

Koukras, A., Dolla, L., & Keppens, R. 2022, in SHINE 2022 Workshop, 68, doi: 10.48550/arXiv.2212.11553

Laming, J. M. 2015, Living Reviews in Solar Physics, 12, 2, doi: 10.1007/lrsp-2015-2

Laming, J. M. 2017, ApJ, 844, 153, doi: 10.3847/1538-4357/aa7cf1

Landi, E., Gruesbeck, J. R., Lepri, S. T., Zurbuchen, T. H., & Fisk, L. A. 2012, ApJ, 761, 48, doi: 10.1088/0004-637X/761/1/48

Leer, E., & Holzer, T. E. 1980, J. Geophys. Res., 85, 4681, doi: 10.1029/JA085iA09p04681

Lemen, J. R., Title, A. M., Akin, D. J., et al. 2012, SoPh, 275, 17, doi: 10.1007/s11207-011-9776-8

Lin, R. P., Anderson, K. A., Ashford, S., et al. 1995, Space Science Reviews, 71, 125, doi: 10.1007/BF00751328

Livi, R., Larson, D. E., Kasper, J. C., et al. 2022, The Astrophysical Journal, 938, 138, doi: 10.3847/1538-4357/ac93f5

Livi, S., Lepri, S. T., Raines, J. M., et al. 2023, A&A, 676, A36, doi: 10.1051/0004-6361/202346304

Macneil, A. R., Owens, M. J., Finley, A. J., & Matt, S. P. 2022, MNRAS, 509, 2390, doi: 10.1093/mnras/stab2965

Mallet, A., & Schekochihin, A. A. 2017, MNRAS, 466, 3918, doi: 10.1093/mnras/stw3251

McComas, D. J., Ebert, R. W., Elliott, H. A., et al. 2008, Geophys. Res. Lett., 35, L18103, doi: 10.1029/2008GL034896

McComas, D. J., Riley, P., Gosling, J. T., Balogh, A., & Forsyth, R. 1998, J. Geophys. Res., 103, 1955, doi: 10.1029/97JA01459

Mostafavi, P., Allen, R. C., McManus, M. D., et al. 2022, The Astrophysical Journal Letters, 926, L38, doi: 10.3847/2041-8213/ac51e1

Neugebauer, M., Liewer, P. C., Smith, E. J., Skoug, R. M., & Zurbuchen, T. H. 2002, Journal of Geophysical Research (Space Physics), 107, 1488, doi: 10.1029/2001JA000306

Nolte, J. T., & Roelof, E. C. 1973, SoPh, 33, 241,
    doi: 10.1007/BF00152395

Nolte, J. T., Krieger, A. S., Timothy, A. F., et al. 1976,
    SoPh, 46, 303, doi: 10.1007/BF00149859

Norton, A., Howe, R., Upton, L., & Usoskin, I. 2023, SSRv,
    219, 64, doi: 10.1007/s11214-023-01008-3

Ohmi, T., Kojima, M., Tokumaru, M., Fujiki, K., &
    Hakamada, K. 2004, Advances in Space Research, 33,
    689, doi: https://doi.org/10.1016/S0273-1177(03)00238-2

Parashar, T. N., Goldstein, M. L., Maruca, B. A., et al.
    2020, The Astrophysical Journal Supplement Series, 246,
    58, doi: 10.3847/1538-4365/ab64e6

Perrone, D., D'Amicis, R., De Marco, R., et al. 2020, A&A,
    633, A166, doi: 10.1051/0004-6361/201937064

Pesnell, W. D., Thompson, B. J., & Chamberlin, P. C.
    2012, SoPh, 275, 3, doi: 10.1007/s11207-011-9841-3

Riley, P., Linker, J. A., & Arge, C. N. 2015, Space
    Weather, 13, 154, doi: 10.1002/2014SW001144

Riley, P., Linker, J. A., & Mikić, Z. 2001, J. Geophys. Res.,
    106, 15889, doi: 10.1029/2000JA000121

Riley, P., & Luhmann, J. G. 2012, SoPh, 277, 355,
    doi: 10.1007/s11207-011-9909-0

Rivera, Y. J., Badman, S. T., & Stevens, M. L. 2024,
    Science

Rivera, Y. J., Raymond, J. C., Landi, E., et al. 2022a, ApJ,
    936, 83, doi: 10.3847/1538-4357/ac8873

Rivera, Y. J., Higginson, A., Lepri, S. T., et al. 2022b,
    Frontiers in Astronomy and Space Sciences, 9, 417,
    doi: 10.3389/fspas.2022.1056347

Schatten, K. H., Wilcox, J. M., & Ness, N. F. 1969, SoPh,
    6, 442, doi: 10.1007/BF00146478

Shi, C., Sioulas, N., Huang, Z., et al. 2023, in AGU Fall
    Meeting Abstracts, Vol. 2023, SH51B–08,
    doi: 10.48550/arXiv.2308.12376

Sioulas, N., Zikopoulos, T., Shi, C., et al. 2024a, arXiv
    e-prints, arXiv:2404.04055,
    doi: 10.48550/arXiv.2404.04055

Sioulas, N., Velli, M., Mallet, A., et al. 2024b, arXiv
    e-prints, arXiv:2407.03649,
    doi: 10.48550/arXiv.2407.03649

Snyder, C. W., & Neugebauer, M. 1966, The Solar Wind
    (Pergamon Press)

Song, H., Cheng, X., Li, L., Zhang, J., & Chen, Y. 2022,
    ApJ, 925, 137, doi: 10.3847/1538-4357/ac3bbf

SPICE Consortium, Anderson, M., Appourchaux, T., et al.
    2020, A&A, 642, A14, doi: 10.1051/0004-6361/201935574

Stakhiv, M., Landi, E., Lepri, S. T., Oran, R., &
    Zurbuchen, T. H. 2015, ApJ, 801, 100,
    doi: 10.1088/0004-637X/801/2/100

Stansby, D., Baker, D., Brooks, D. H., & Owen, C. J. 2020a,
    A&A, 640, A28, doi: 10.1051/0004-6361/202038319

Stansby, D., Green, L. M., van Driel-Gesztelyi, L., &
    Horbury, T. S. 2021, Solar Physics, 296, 116,
    doi: 10.1007/s11207-021-01861-x

Stansby, D., Horbury, T. S., & Matteini, L. 2018, Monthly
    Notices of the Royal Astronomical Society, 482, 1706,
    doi: 10.1093/mnras/sty2814

Stansby, D., Matteini, L., Horbury, T. S., et al. 2020b,
    MNRAS, 492, 39, doi: 10.1093/mnras/stz3422

Stansby, D., Yeates, A., & Badman, S. 2020, Journal of
    Open Source Software, 5, 2732, doi: 10.21105/joss.02732

Stansby, D., Rai, Y., Argall, M., et al. 2022

Virtanen, P., Gommers, R., Oliphant, T. E., et al. 2020,
    Nature Methods, 17, 261, doi: 10.1038/s41592-019-0686-2

von Steiger, R., Schwadron, N. A., Fisk, L. A., et al. 2000,
    Journal of Geophysical Research: Space Physics, 105,
    27217, doi: https://doi.org/10.1029/1999JA000358

Wallace, S., Arge, C. N., Viall, N., & Pihlström, Y. 2020,
    The Astrophysical Journal, 898, 78,
    doi: 10.3847/1538-4357/ab98a0

Wang, Y. M., Grappin, R., Robbrecht, E., & Sheeley,
    N. R., J. 2012, ApJ, 749, 182,
    doi: 10.1088/0004-637X/749/2/182

Wang, Y.-M., Ko, Y.-K., & Grappin, R. 2009, The
    Astrophysical Journal, 691, 760,
    doi: 10.1088/0004-637X/691/1/760

Wang, Y. M., & Sheeley, N. R., J. 1990, ApJ, 355, 726,
    doi: 10.1086/168805

—. 1997, Geophys. Res. Lett., 24, 3141,
    doi: 10.1029/97GL53305

—. 2003, ApJ, 587, 818, doi: 10.1086/368302

Weber, M. A., Schunker, H., Jouve, L., & Işık, E. 2023,
    Space Science Reviews, 219, 63,
    doi: 10.1007/s11214-023-01006-5

Wes McKinney. 2010, in Proceedings of the 9th Python in
    Science Conference, ed. Stéfan van der Walt & Jarrod
    Millman, 56 – 61, doi: 10.25080/Majora-92bf1922-00a

Worden, J., & Harvey, J. 2000, Solar Physics, 195, 247,
    doi: 10.1023/A:1005272502885

Yardley, S. L., Brooks, D. H., D'Amicis, R., et al. 2024,
    Nature Astronomy, doi: 10.1038/s41550-024-02278-9